ARMY RESEARCH LABORATORY

Coupling Between CTH and LS-DYNA for Thermal Postprocessing: Application to Propellant Cookoff From a Residual Penetrator

by Martin N. Raftenberg, Hubert W. Meyer, Jr., and Jerry A. Clarke

ARL-TR-3924   September 2006

NOTICES

Disclaimers

Army Research Laboratory

Aberdeen Proving Ground, MD 21005-5066

Coupling Between CTH and
LS-DYNA for Thermal Postprocessing: Application to
Propellant Cookoff From a Residual Penetrator

Martin N. Raftenberg, Hubert W. Meyer, Jr., and Jerry A. Clarke
Weapons and Materials Research Directorate, ARL

1. REPORT DATE (DD-MM-YYYY)	2. REPORT TYPE	3. DATES COVERED (From - To)
September 2006	Final	October 2005–July 2006

4. TITLE AND SUBTITLE	5a. CONTRACT NUMBER
Coupling Between CTH and LS-DYNA for Thermal Postprocessing: Application to Propellant Cookoff From a Residual Penetrator	
	5b. GRANT NUMBER
	5c. PROGRAM ELEMENT NUMBER

6. AUTHOR(S)	5d. PROJECT NUMBER
Martin N. Raftenberg, Hubert W. Meyer, Jr., and Jerry A. Clarke	
	5e. TASK NUMBER
	5f. WORK UNIT NUMBER

7. PERFORMING ORGANIZATION NAME(S) AND ADDRESS(ES)	8. PERFORMING ORGANIZATION REPORT NUMBER
U.S. Army Research Laboratory ATTN: AMSRD-ARL-WM-TD Aberdeen Proving Ground, MD 21005-5066	ARL-TR-3924

9. SPONSORING/MONITORING AGENCY NAME(S) AND ADDRESS(ES)	10. SPONSOR/MONITOR'S ACRONYM(S)
	11. SPONSOR/MONITOR'S REPORT NUMBER(S)

12. DISTRIBUTION/AVAILABILITY STATEMENT

Approved for public release; distribution is unlimited.

13. SUPPLEMENTARY NOTES

14. ABSTRACT

A procedure was developed for performing a postprocessing heat conduction analysis from a CTH solution for a residual penetrator's shape and temperature field. LS-DYNA was employed for the heat conduction analysis. The interface between CTH and LS-DYNA involved the codes EnSight and HyperMesh. The procedure was applied to perforation of a titanium plate by a steel right circular cylinder at 433 m/s, followed by cookoff of an M30A1 grain by contact with the hot steel residual. The temperature field as a function of time within the M30A1 grain was compared with published data for initiation time as a function of temperature. In an appendix, an analytical solution for heat conduction between two semi-infinite layers is used to assess mesh adequacy in the residual-propellant simulation.

15. SUBJECT TERMS

heat conduction, M30, LS-DYNA, propellant cookoff, plastic work, CTH

16. SECURITY CLASSIFICATION OF:			17. LIMITATION OF ABSTRACT	18. NUMBER OF PAGES	19a. NAME OF RESPONSIBLE PERSON Martin N. Raftenberg
a. REPORT	b. ABSTRACT	c. THIS PAGE	UL	56	19b. TELEPHONE NUMBER (Include area code)
UNCLASSIFIED	UNCLASSIFIED	UNCLASSIFIED			410-306-0949

Contents

List of Figures

List of Tables

Acknowledgments

INTENTIONALLY LEFT BLANK.

1. Introduction

We considered the following scenario: A steel projectile perforates a sheet of titanium armor and is heated by plastic work during the penetration process. The hot steel residual then comes to rest in a bed of M30A1 propellant. The subsequent temperature rise in the propellant, if of sufficient magnitude and duration, can lead to initiation (*1*).

Our goal was to develop a computational methodology to study this scenario. Section 2 describes our application of the CTH Eulerian hydrocode (*2*) to the steel-titanium penetration problem. Section 3 describes our application of EnSight (*3*) to the extraction from the resulting CTH Spyplot output files the geometry of and temperature field within the steel residual. Section 4 then describes our use of LS-DYNA (*4*) to study heat conduction from the residual to a single grain of M30A1 propellant. Section 5 concludes with a summary and assessment.

2. Titanium Perforation Simulation With CTH

2.1 Problem Definition

A right circular cylinder (RCC) of 4340 steel impacts a titanium plate at normal incidence and a speed of 433 m/s (figure 1). The RCC has a length and diameter of 20 mm. The target plate has a thickness of 6.35 mm and a square face with 127-mm edge length.

2.2 Meshing

The stationary (Eulerian) mesh consisted of 6.24M cells, each a cube of 0.635-mm edge length. In terms of the coordinate system defined in figure 1, the *x*-length of the mesh was 95.25 mm, and the *y*- and *z*-lengths were each 129.54 mm. Symmetry boundary conditions were not employed.

2.3 Material Properties

The projectile was composed of martensitic 4340 steel. The target plate was composed of the titanium alloy Ti-6Al-4V. The material models used are described next. The values assigned to all material constants are given in table 1. For most parameters, the source of the value is also given in the table. For the others, there is more uncertainty in the value.
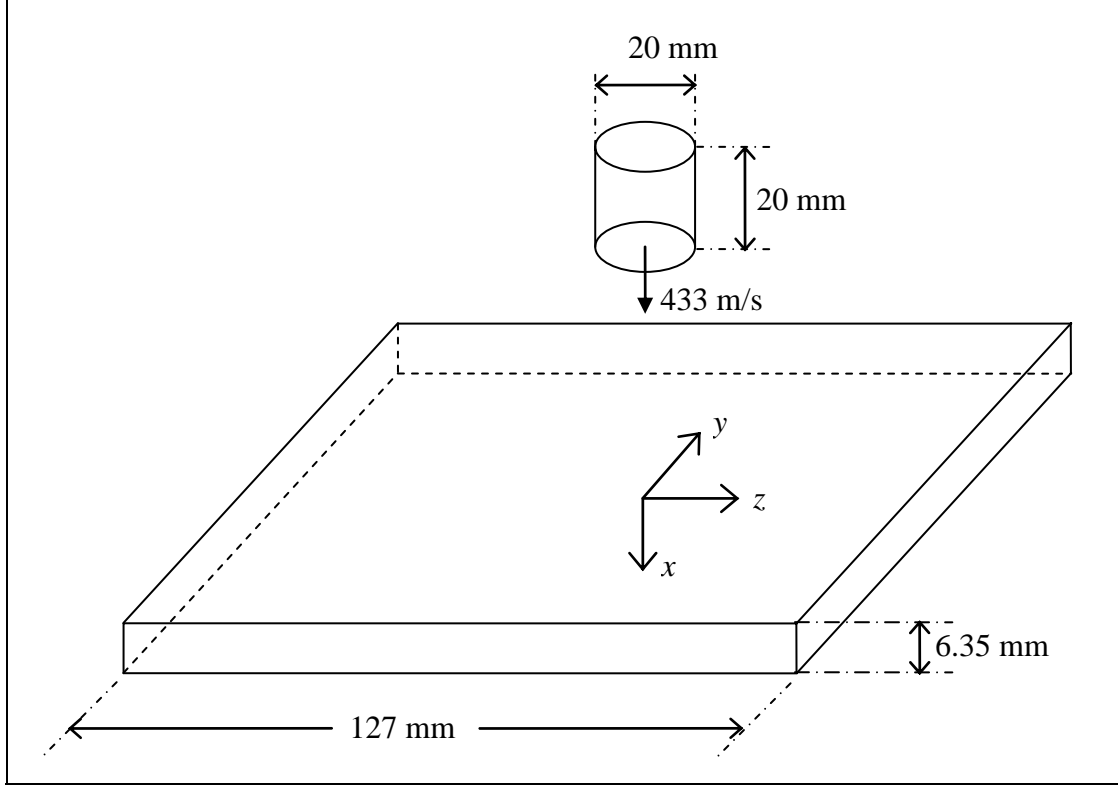
Figure 1. An RCC of 4340 steel strikes the center of a square titanium plate at normal incidence and 433 m/s. (The drawing is not to scale.)

2.3.1 Equation of State

The dilatational response of the 4340 steel and the titanium were both modeled by a Mie-Grüneisen equation of state with a constant Grüneisen coefficient, γ_0. The shock Hugoniot curve was described by the linear relationship between the shock speed, U_S, and the particle speed, u_P,

$$U_S = C_S + S u_P . \tag{1}$$

Here, C_S is the sound speed and S is a material constant. Note in table 1 that the titanium alloy was assigned properties obtained for aluminum.

2.3.2 Strength

The titanium's strength was represented with the FCC form of the Zerilli-Armstrong model (5), according to which

$$Y = C_0 + C_1 \exp\left(- C_3 \theta + C_4 \theta \ln \dot{\varepsilon}\right) + C_5 \varepsilon^n . \tag{2}$$

2

Table 1. Material properties in the section 2 CTH calculations.

	4340 Steel	Ti-6Al-4V
ρ (kg/m^3)	7850 (6, 7, 8, 9)	2660 (8) for Al
γ_0	2.17	1.97 (8) for Al
C_S (m/s)	4570 (8)	5220 (8, 9) for Al
S	1.49 (9)	1.37 (8, 9) for Al
c_p (J/kg·K)	475 (6, 7)	896 (6) for Al
ν	0.29 (7)	0.30
C_0 (GPa)	—	1.116
C_1 (GPa)	—	0.24 (10)
C_3 (1/K)	—	0.0024 (10)
C_4 (1/K)	—	0.0043 (10)
C_5 (GPa)	—	0.656 (10)
n	—	0.50 (10)
A (GPa)	0.72 (11)	—
B (GPa)	0.78 (11)	—
C	0.004 (11)	—
M	1.00 (11)	—
N	0.106 (11)	—
θ_m (K)	1782 (6, 7)	—
θ_r (K)	294	—
D_1	See (12)	See (12)
D_2	See (12)	See (12)
D_3	See (12)	See (12)
D_4	0.002 (7)	See (12)
D_5	0.61 (7)	See (12)
P_{frac} (GPa)	−2.5	−5.9

Here, Y is the yield stress, θ the temperature, ε the equivalent plastic strain, and $\dot{\varepsilon}$ the time rate of change of equivalent plastic strain nondimensionalized by a reference rate of 1/s. The model introduces six material constants: C_0, C_1, C_3, C_4, C_5, and n.

The steel's strength was represented with the Johnson-Cook strength model (6), according to which

$$Y = \left[A + B(\varepsilon^p)^N\right]\left[1 + C \ln \dot{\varepsilon}\right]\left[1 - \left(\theta^*\right)^M\right].$$ (3)

In equation 3, θ^* is the homologous temperature, defined by

$$\theta^* = \frac{\theta - \theta_r}{\theta_m - \theta_r},$$ (4)

where θ_r is the room temperature and θ_m is the material's melting temperature. The seven material constants are A, B, C, N, M, θ_m, and θ_r. In addition Poisson's ratio, ν, is used to compute elastic strains.

2.3.3 Damage

The Johnson-Cook fracture model (7) was applied to both 4340 steel and Ti-6Al-4V. This model introduces a fracture strain, ε_f, which is related to the local stress, strain rate, and temperature according to

$$\varepsilon_f = \left[D_1 + D_2 \exp\left(D_3 \sigma^* \right) \right] \left[1 + D_4 \ln \dot{\varepsilon} \right] \left[1 + D_5 \theta^* \right] , \tag{5}$$

where

$$\sigma^* = -\frac{P}{\sigma_{eq}} . \tag{6}$$

Here, P is pressure, σ_{eq} is the von Mises stress, and ε and $\dot{\varepsilon}$ are again equivalent plastic strain and the dimensionless rate of change of equivalent plastic strain, respectively. The Johnson-Cook fracture model introduces five material constants, D_1, D_2, D_3, D_4, and D_5.

In addition, CTH offers the ability to insert void in cells that exhibit pressure less than or equal to a prescribed value, P_{frac}. This feature was applied to both metals, with the P_{frac} values in table 1. The negative values indicate tension.

2.4 Results

Heat conduction was neglected in the CTH perforation calculations. The temperature rise in a cell during a given time step was calculated by dividing work increment by specific heat. The results for volume fraction and temperature of steel in each cell were written to Spyplot files called "spcth." These are the solution variables needed for the thermal postprocessing with LS-DYNA.

Figures 2 and 3 show the regions of steel and titanium at intervals of 20 µs. These regions were identified based on a material volume fraction of 0.5 or greater. The problem was terminated at 200 µs after impact.

2.5 Discussion

The problem in figure 1 was studied experimentally by Kyle Bates of the U.S. Army Research Laboratory's Survivability/Lethality Analysis Directorate. In the experiment, the recovered titanium plug and steel residual were bounded by shiny surfaces (13) indicative of plastic flow and possibly adiabatic shear banding. In the CTH simulation, damage in the two metals was modeled with Johnson-Cook fracture. It has not been established that this damage model
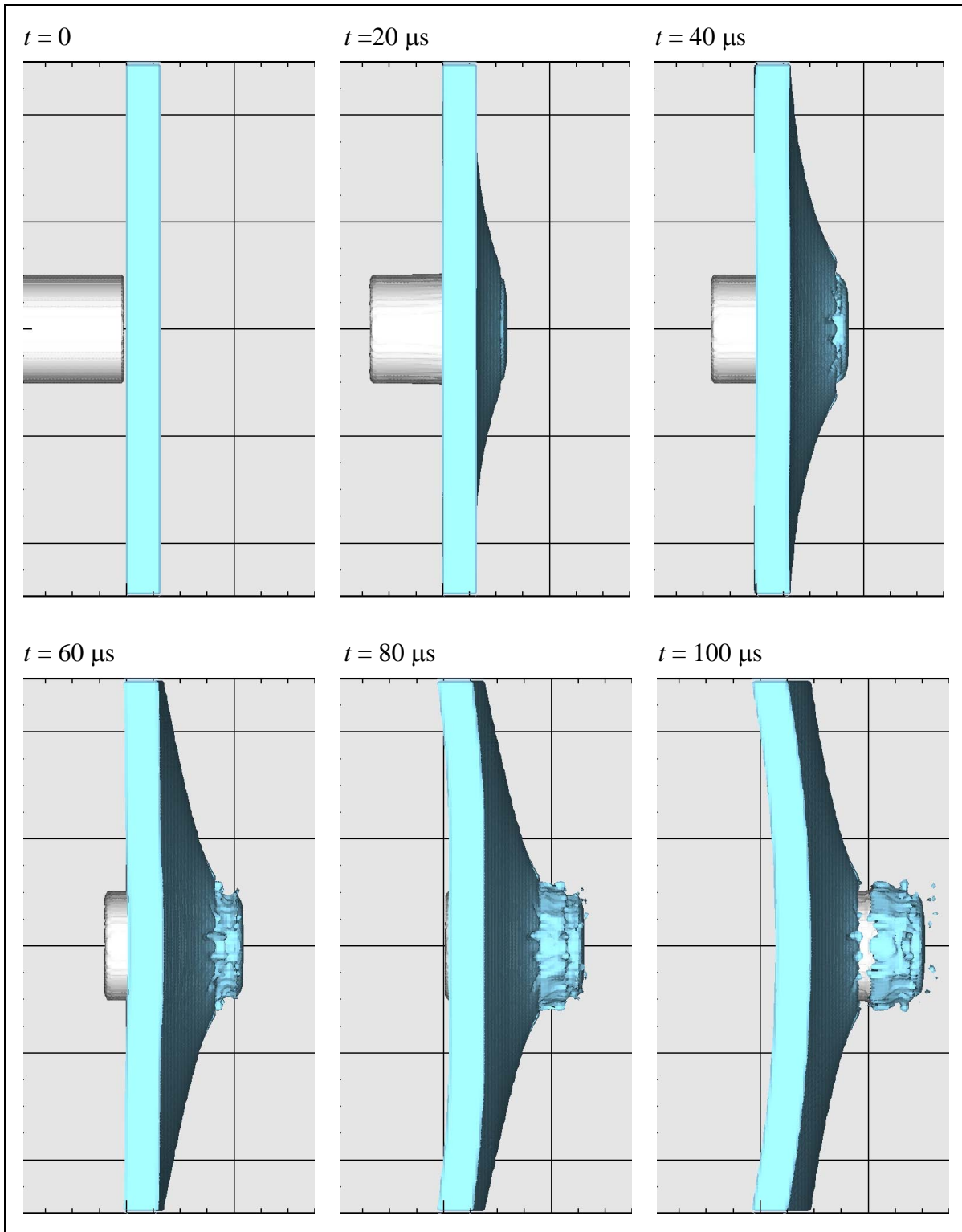
Figure 2. CTH output for the steel vs. titanium at $t = 0$ to 100 μs after impact.
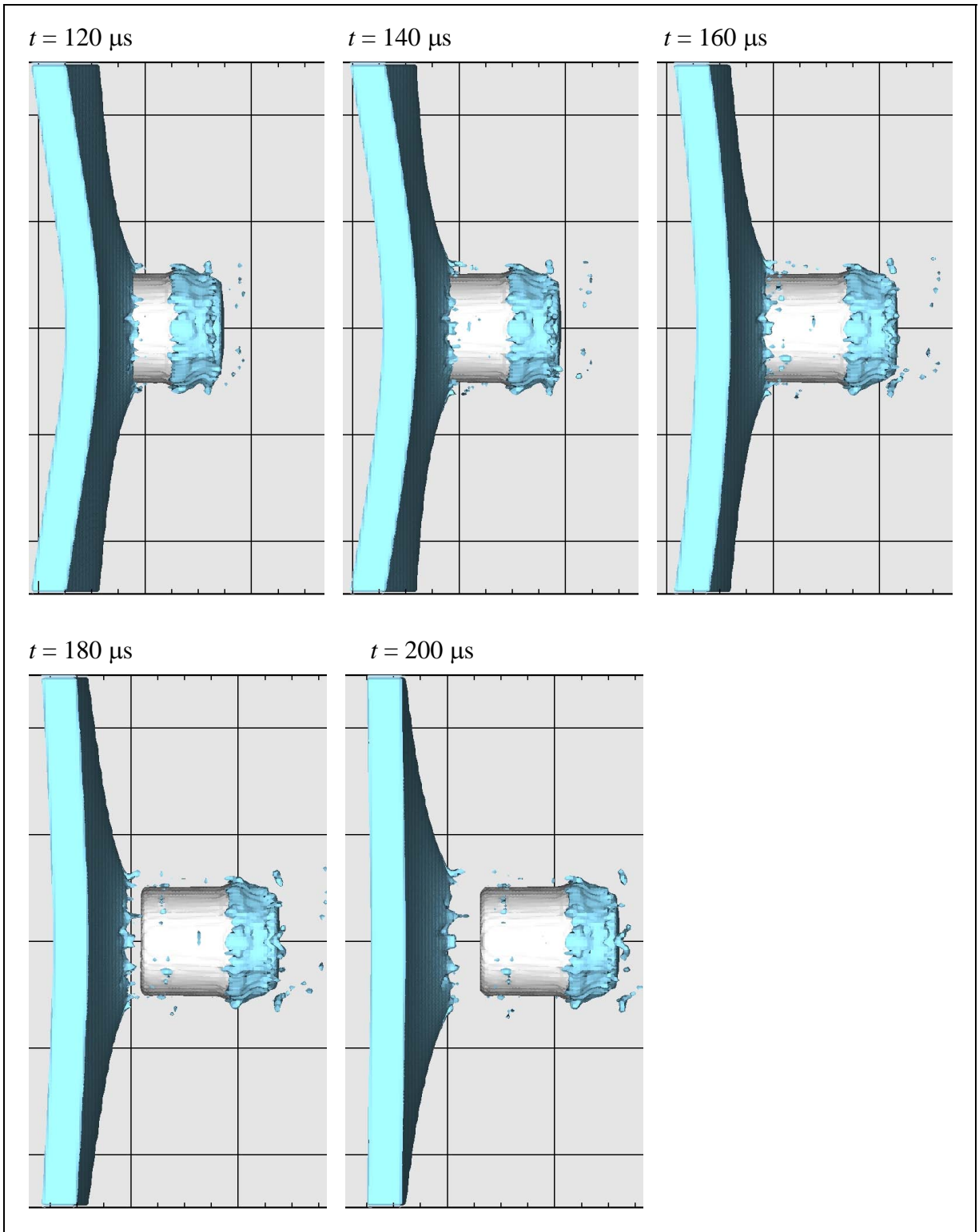
Figure 3. CTH output for the steel vs. titanium at t = 120 to 200 μs after impact.

introduces effects of adiabatic shear localization. An effect of plug-bounding shear localization in the titanium target is to reduce the work needed to perforate the target. Thus, the computed plastic work and temperature rise in the steel projectile are likely to overestimate the actual values.

As noted in section 2.3.1, we applied to the titanium alloy values for equation of state constants that were obtained for aluminum. This was another source of error.

3. Extraction of Residual Geometry and Temperature Field Using EnSight

The spcth files were read with EnSight (figure 4). This software enabled identification of those CTH cells that exhibited a steel volume fraction of 0.5 or greater. This criterion was only satisfied by the single closed volume of cells shown in figure 5. We identified this region as the steel residual.

CTH specifies temperature at the centroid of each cell. EnSight was used to interpolate temperatures to the eight vertex nodes of each cell. The temperature field is shown in figures 6 and 7. The former shows temperature on the outer boundary of the steel residual, the latter shows temperature in the interior exposed by a diametral cut.

EnSight was used to create three ascii files:

1. Element cards
    Each line consists of nine integers: a unique number assigned to each CTH cell that satisfied the 0.5 volume fraction steel criterion, followed by eight numbers identifying each of the cell's vertex nodes.

2. Node cards
    Each line contains four quantities: the integral node number and the x, y, and z coordinates of that node.

3. Initial nodal temperatures
    Each line consists of the integer identifying a vertex node deemed to be part of the residual, followed by its initial temperature in Kelvin.

These three sets of cards were brought into LS-DYNA Keyword format and then combined to form part of a Keyword input file. The latter was then brought into HyperMesh (*14*), a software product used to preprocess for LS-DYNA. The remainder of the LS-DYNA input file was then created within HyperMesh. This remainder consists specifically of the mesh for the M30A1 propellant, the descriptions of the steel and M30A1 thermal material properties, the thermal boundary conditions, and the termination time, time step, and thermal solver specification.
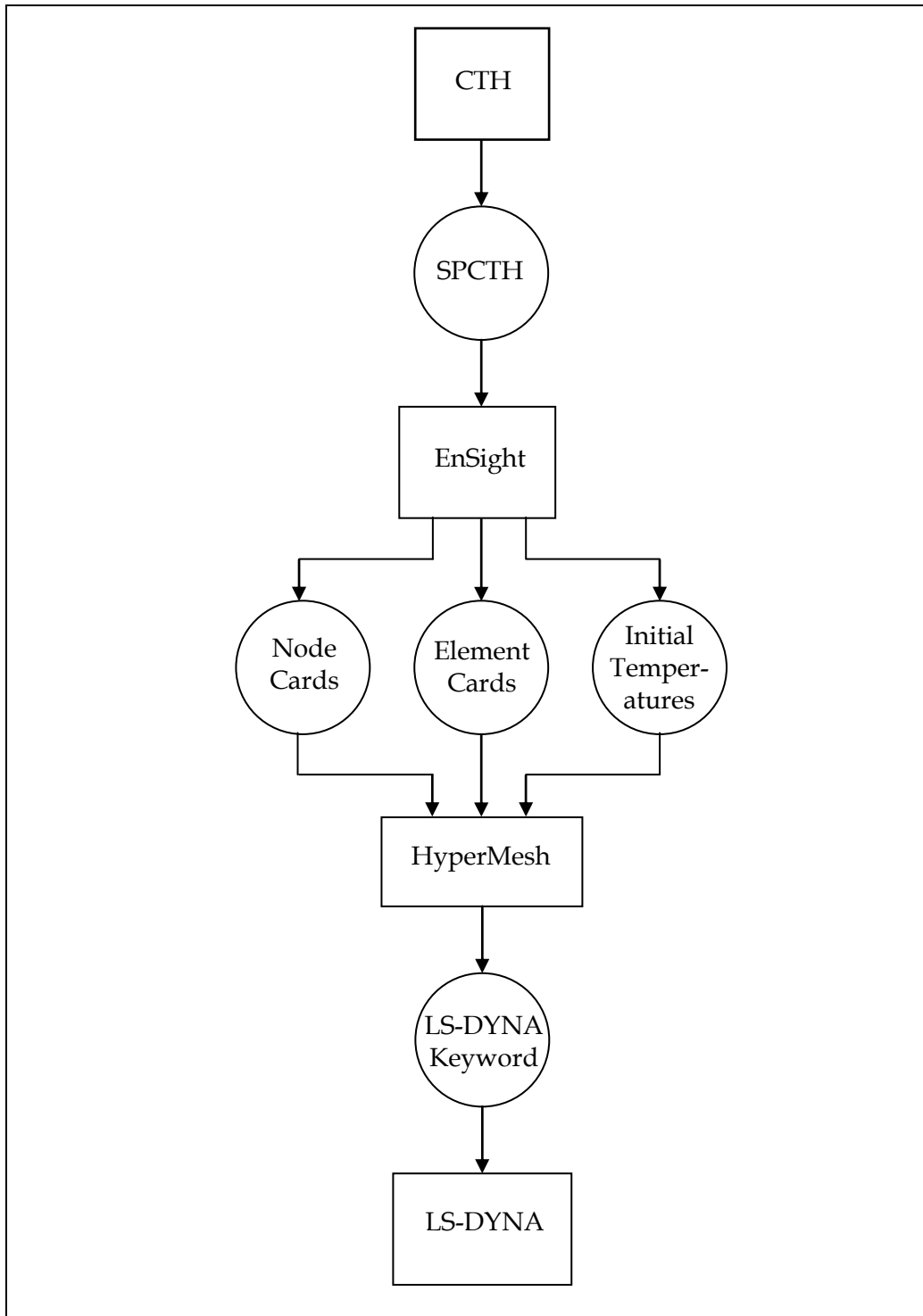
Figure 4. Overview of computations.
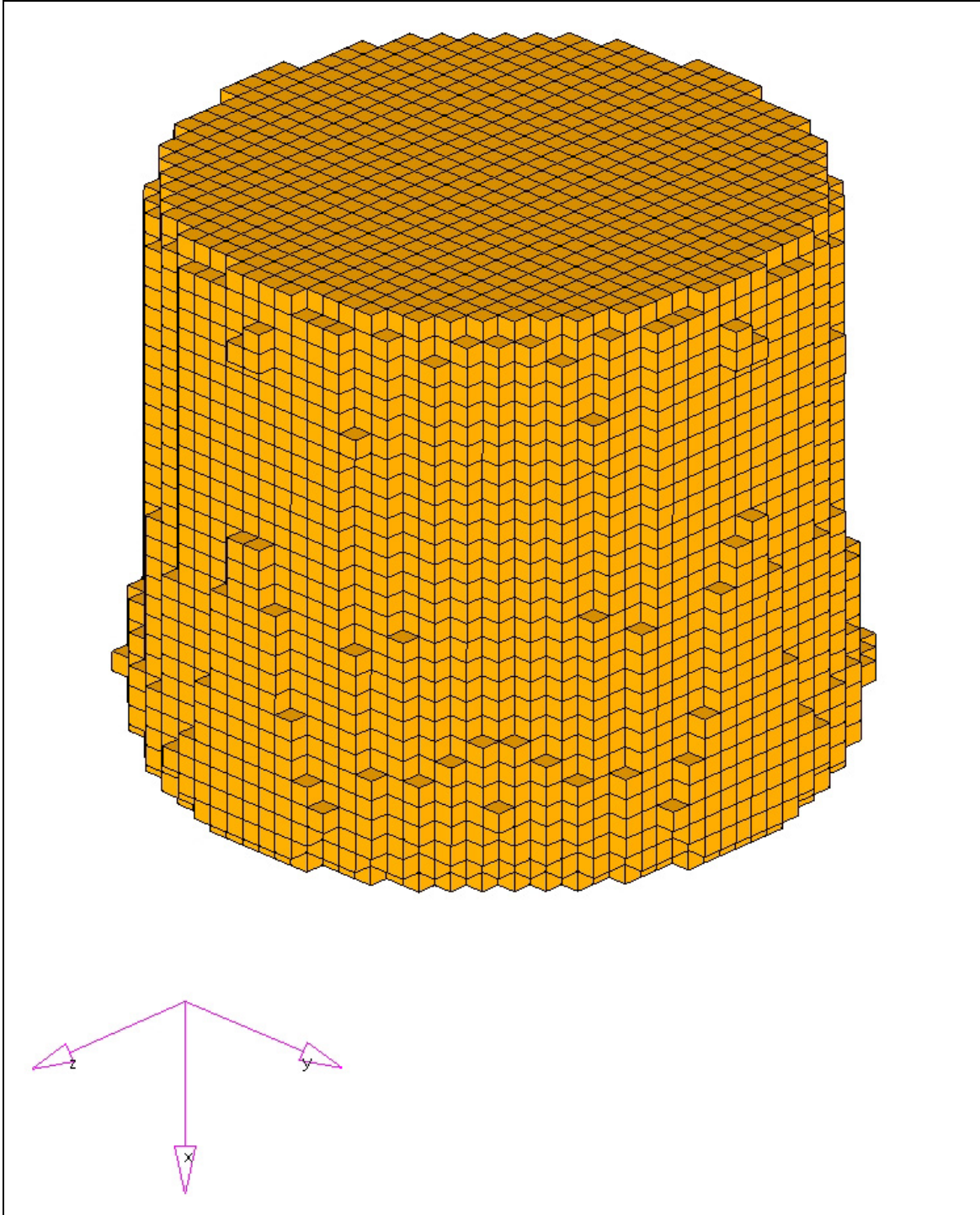
Figure 5. The CTH cells that at $t = 200$ µs are identified with the steel residual.
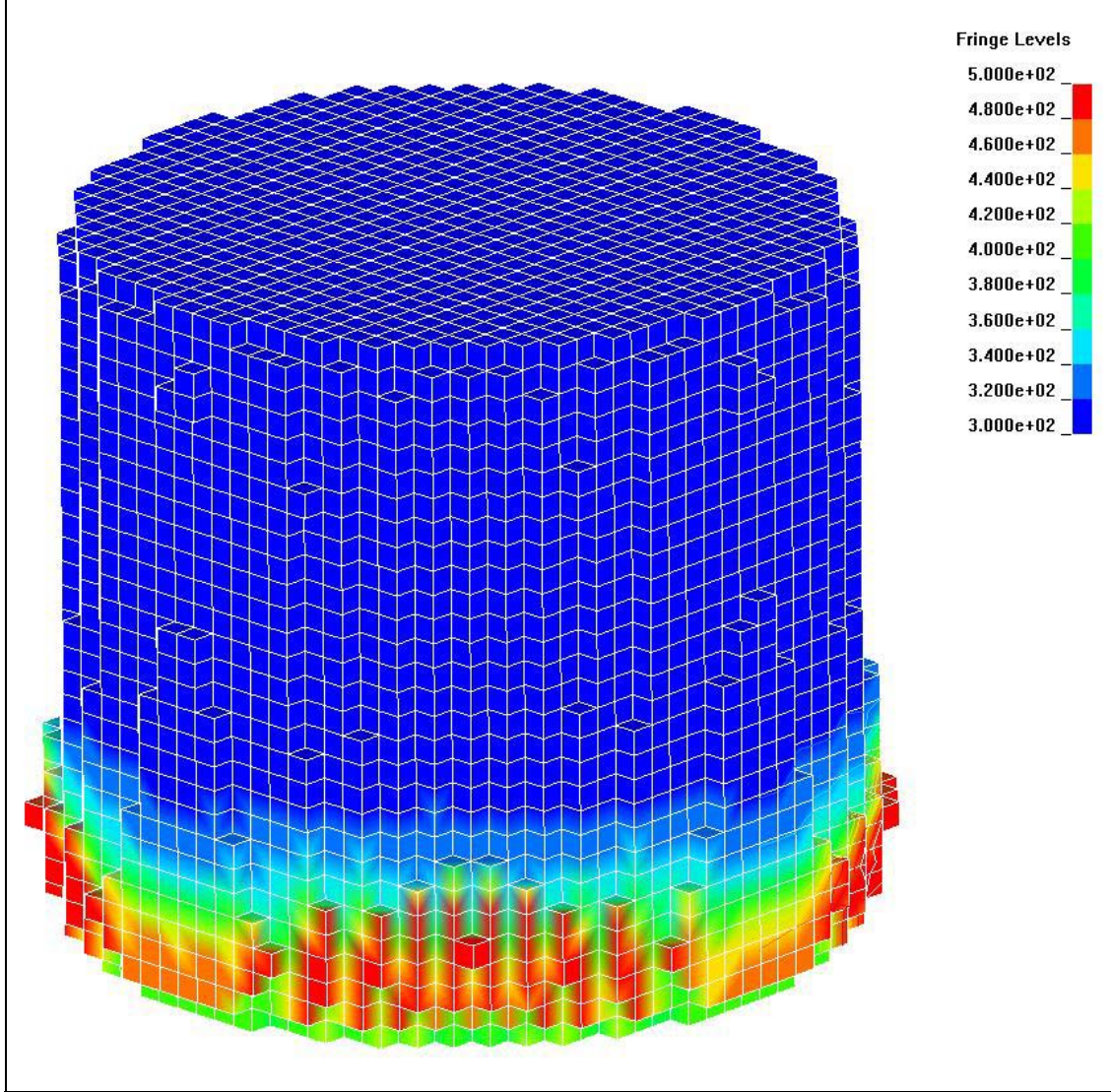
Figure 6. CTH results for temperature contours in the steel residual at $t = 200$ µs; these temperature results are applied as initial condition in the LS-DYNA analysis. (The fringe levels are in Kelvin.)

4. Residual and Propellant Heat Conduction Analysis With LS-DYNA

4.1 Problem Definition

Horst et al. (*15*) describes the geometry of individual grains of M30A1 as RCCs with diameters of 10.6 mm and lengths of 24.4 mm. We considered a single grain composed of a homogeneous material and placed in direct contact with a hot section of the steel residual. A Lagrangian finite-element (FE) model was created for this grain. We assumed that all mechanical deformation,
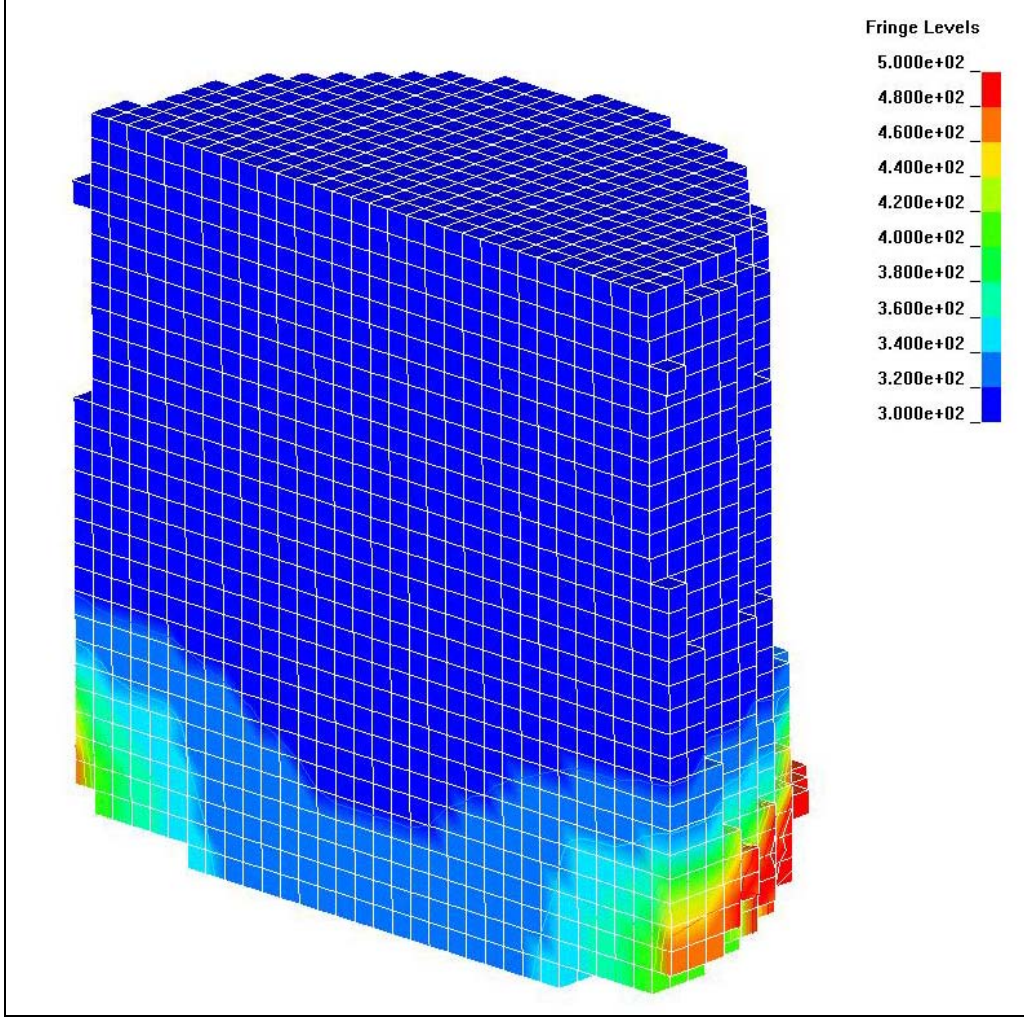
Figure 7. The steel residual in figure 6 is sectioned along an approximate diameter to reveal the internal temperature field. (The fringe levels are in Kelvin.)

including thermal expansion and remaining stress waves, are negligible in the subsequent heat transfer to the M30A1 grain once the steel residual has come to rest. This allowed for the use of LS-DYNA in an implicit heat conduction mode. We assumed perfect thermal contact between the steel residual and the M30A1 grain.

Let Ω_1 and Ω_2 be the regions of space occupied by the steel residual and the M30A1 grain, respectively. Let $\theta_1(\mathbf{x}, t)$ and $\theta_2(\mathbf{x}, t)$ be the temperature fields within the steel residual and the M30A1 grain, respectively. Heat flow is then governed by the equations

$$\frac{\partial \theta_1}{\partial t} = \alpha_1 \nabla^2 \theta_1 ; \ \mathbf{x} \in \Omega_1, \ t > 0 \tag{7}$$

and

$$\frac{\partial \theta_2}{\partial t} = \alpha_2 \nabla^2 \theta_2 ; \ \mathbf{x} \in \Omega_2, \ t > 0, \tag{8}$$

11

in which α_1 and α_2 are the thermal diffusivities of steel and M30A1, respectively. These are defined by

$$\alpha_1 = \frac{\kappa_1}{\rho_1 c_{p1}} \tag{9}$$

and

$$\alpha_2 = \frac{\kappa_2}{\rho_2 c_{p2}}. \tag{10}$$

Here, κ_1 ad κ_2 are the thermal conductivities, ρ_1 and ρ_2 are the densities, and c_{p1} and c_{p2} are the constant-pressure specific heats for the steel and the M30A1 grain, respectively. These conductivities, densities, and specific heats were assumed to be material constants, independent of temperature.

The initial conditions are

$$\theta_1(\mathbf{x},0) = \theta_0(\mathbf{x}); \ \mathbf{x} \in \Omega_1 \tag{11}$$

and

$$\theta_2(\mathbf{x},0) = \theta_r = 294\,\mathrm{K}; \ \mathbf{x} \in \Omega_2, \tag{12}$$

where $\theta_0(\mathbf{x})$ is the initial temperature field within the steel residual. This temperature field is identified with the CTH output shown in figures 6 and 7. θ_r is room temperature.

The imposed boundary conditions are indicated schematically in figure 8. Along the interface between steel and propellant, perfect thermal contact is assumed, so that temperature and heat flux are both continuous.

$$\theta_1(\mathbf{x},t) = \theta_2(\mathbf{x},t); \ \mathbf{x} \in \Omega_1 \cup \Omega_2, \ t > 0. \tag{13}$$

$$\kappa_1 \frac{\partial \theta_1(\mathbf{x},t)}{\partial n_1} = -\kappa_2 \frac{\partial \theta_2(\mathbf{x},t)}{\partial n_2}; \ \mathbf{x} \in \Omega_1 \cup \Omega_2, \ t > 0. \tag{14}$$

Here, n_1 and n_2 indicate the directions of the outer normal to the boundary of the steel residual and propellant grain, respectively. Throughout the portions of the steel and propellant boundaries not in mutual contact, an insulation boundary condition is assumed. Let $\partial \Omega_{1,\mathrm{ins}}$ and $\partial \Omega_{2,\mathrm{ins}}$ be these insulated sections of the steel and propellant boundaries, respectively. Then,

$$\frac{\partial \theta_1(\mathbf{x},t)}{\partial n_1} = 0; \ \mathbf{x} \in \partial \Omega_{1,\mathrm{ins}}, \ t > 0 \tag{15}$$

and

$$\frac{\partial \theta_2(\mathbf{x},t)}{\partial n_2} = 0; \ \mathbf{x} \in \partial \Omega_{2,\mathrm{ins}}, \ t > 0. \tag{16}$$

12
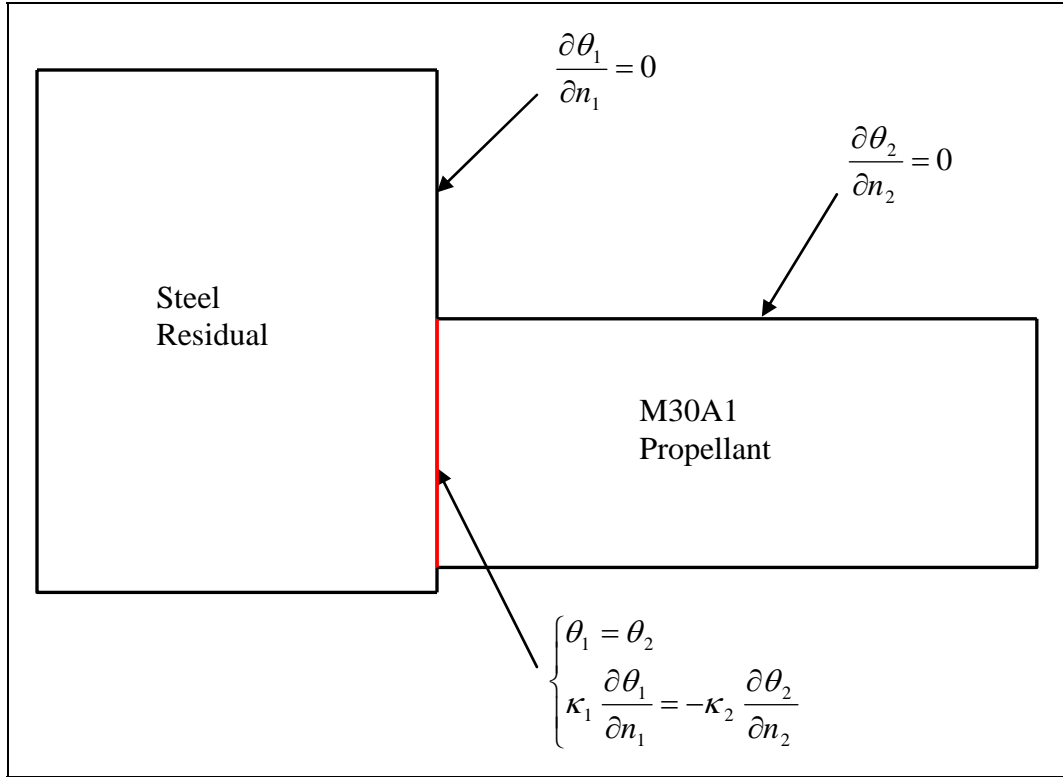
Figure 8. Schematic of the boundary conditions applied in the heat conduction analysis of section 4. Temperature and heat flux are continuous along the residual-propellant interface; heat flux is zero elsewhere along the residual and propellant boundaries.

4.2 Material Properties

The applicable material properties for this heat conduction analysis are density, specific heat, thermal conductivity, and thermal diffusivity. Only three are independent, with the fourth related by equation 9 or 10.

Values for these material constants in the case of 4340 steel are listed in table 2. The source of each value is indicated.

Table 2. Material constants for steel and propellant.

	4340 Steel	**M30A1**
ρ (kg/m^3)	7823 (*6, 7, 8, 9*)	2000
c_{p} (J/kg·K)	477.8 (*6, 7*)	1100 (equation 10)
κ (W/m·K)	38.11 (*7*)	0.418 (*16*)
α (m^2/s)	1.020×10^{-5} (equation 9)	1.9×10^{-7} (*16*)

Miller (*16*) measured thermal conductivity and thermal diffusivity of a grain of M30A1 as functions of temperature and direction. His data have been converted to SI units and reproduced in table 3. "M3$\tilde{0}_{//}$" and "M3$\tilde{0}_{\perp}$" indicate properties along and orthogonal to the axis of the grain, respectively. For both κ and α, measurements were generally larger along the grain axis. Since κ and α were both modeled as independent of temperature and direction in the LS-DYNA simulations, a representative value for each quantity was used (see table 2). Specific heat was then determined from equation 10.

Table 3. Thermal conductivity and diffusivity of an M30 grain (reproduced from Miller [*16*]).

	M3$\tilde{0}_{\perp}$		M3$\tilde{0}_{//}$	
θ (K)	κ (W/m·K)	a ($\times 10^{-7}$ m^2/s)	κ (W/m·K)	a ($\times 10^{-7}$ m^2/s)
254	n.d.	n.d.	0.419 ± 0.021	2.34 ± 0.09
255	0.329 ± 0.007	1.78 ± 0.03	n.d.	n.d.
275	0.352 ± 0.010	1.74 ± 0.04	n.d.	n.d.
276	n.d.	n.d.	0.486 ± 0.029	2.41 ± 0.14
295	n.d.	n.d.	0.427 ± 0.025	1.90 ± 0.09
296	n.d.	n.d.	0.448 ± 0.025	2.09 ± 0.11
297	0.320 ± 0.033	1.46 ± 0.11	n.d.	n.d.
321	0.325 ± 0.022	1.39 ± 0.08	n.d.	n.d.
322	n.d.	n.d.	0.412 ± 0.016	1.88 ± 0.04

Note: n.d. = no data.

4.3 Meshing

The Eulerian mesh of the CTH output was converted directly into Lagrangian FEs. Each steel FE was a cubic 8-node brick with a 0.635-mm edge length (figure 5).

The new mesh created for the cylindrical M30A1 grain also consisted entirely of cubic 8-node bricks with a 0.635-mm edge length (figures 9 and 10). HyperMesh was used in creating this mesh.

An end face of the M30A1 mesh was placed in contact with a flat region on the periphery of the steel residual (see figures 10, 11, and 12). This flat region of the residual was comprised of a face of each of 83 elements and formed a substantial contact surface for the propellant grain. Note, however, that this flat region of the residual did not coincide with the region in which CTH determined temperatures to be the greatest. The vertex nodes for each of these 83 steel element faces shown in figure 11 were shared by the 83 propellant element faces shown in figure 10. In this way, the continuity of temperature and heat flux across the residual-grain interface (equations 13 and 14) was imposed.

4.4 Results and Discussion

The computed temperature fields at 1 and 2 s after contact are shown in figures 13 and 14. The latter figure is a diametral section to reveal the internal field. Since the thermal diffusivity of steel is two orders of magnitude larger than that of M30, heat flows more rapidly within the steel than from the steel to the propellant.

R = 5.3 mm
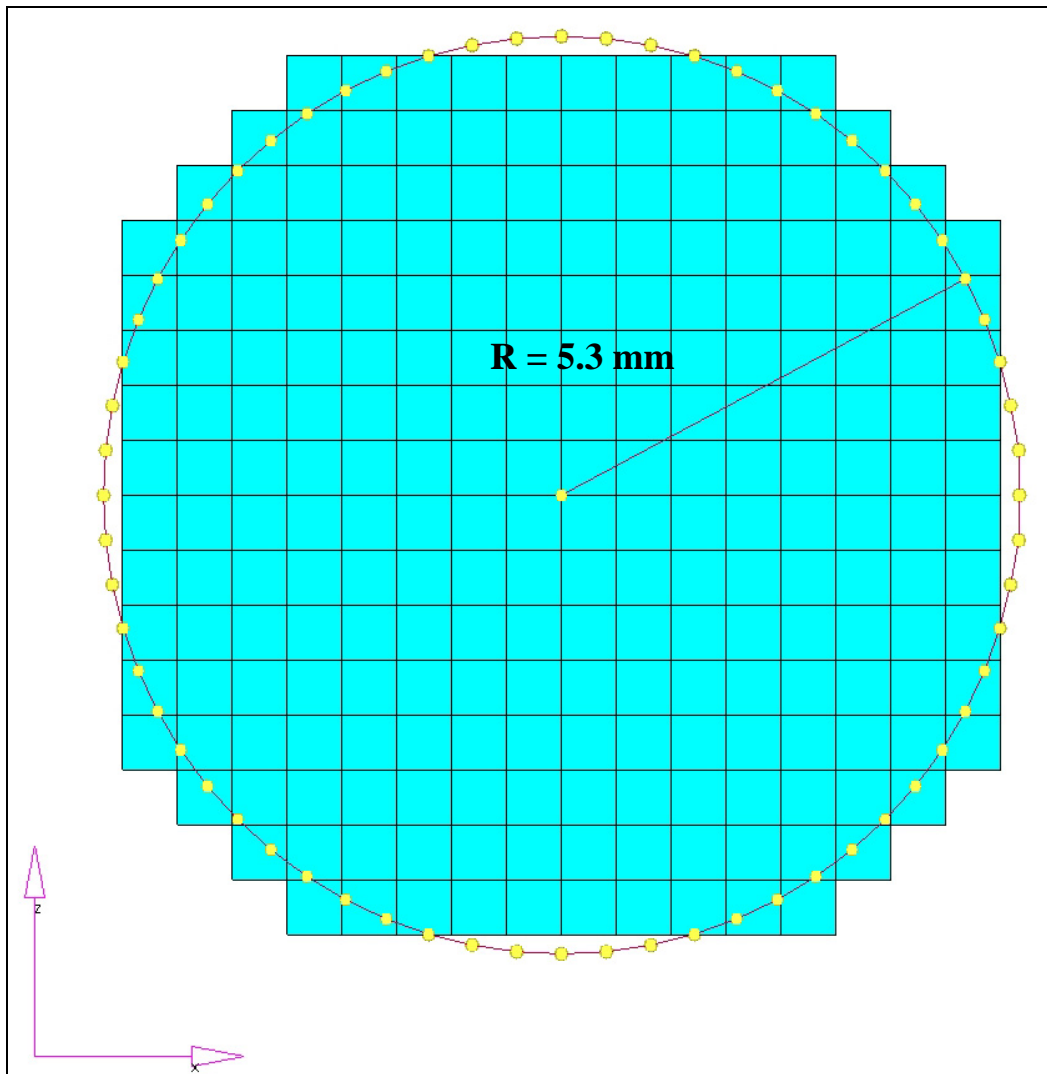
Figure 9. The FE mesh used to represent the circular cross section of an M30A1 grain.
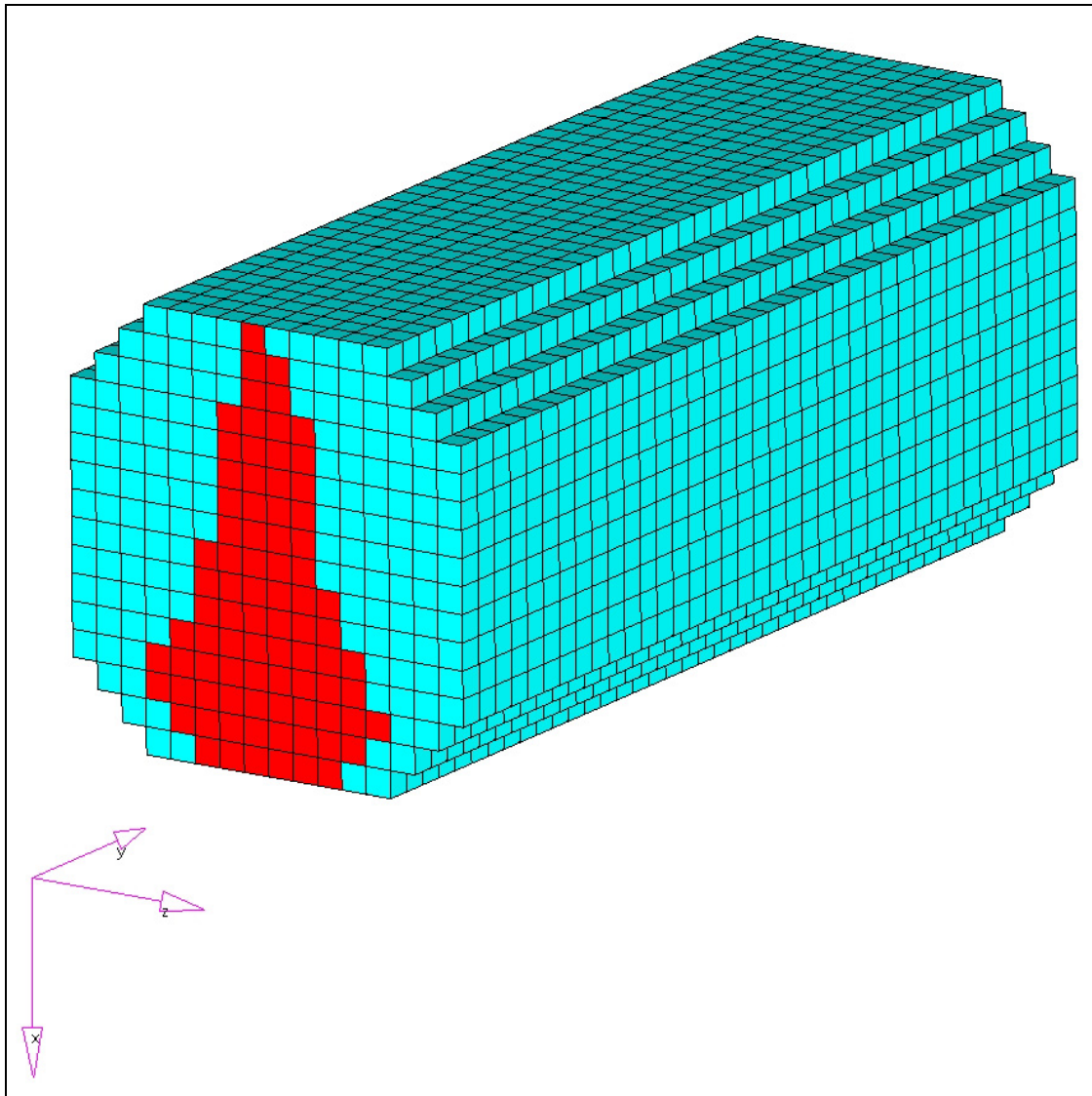
Figure 10. The entire mesh for an M30A1 grain. A face of each of 83 M30 elements, colored red, was contiguous with the steel-residual mesh.
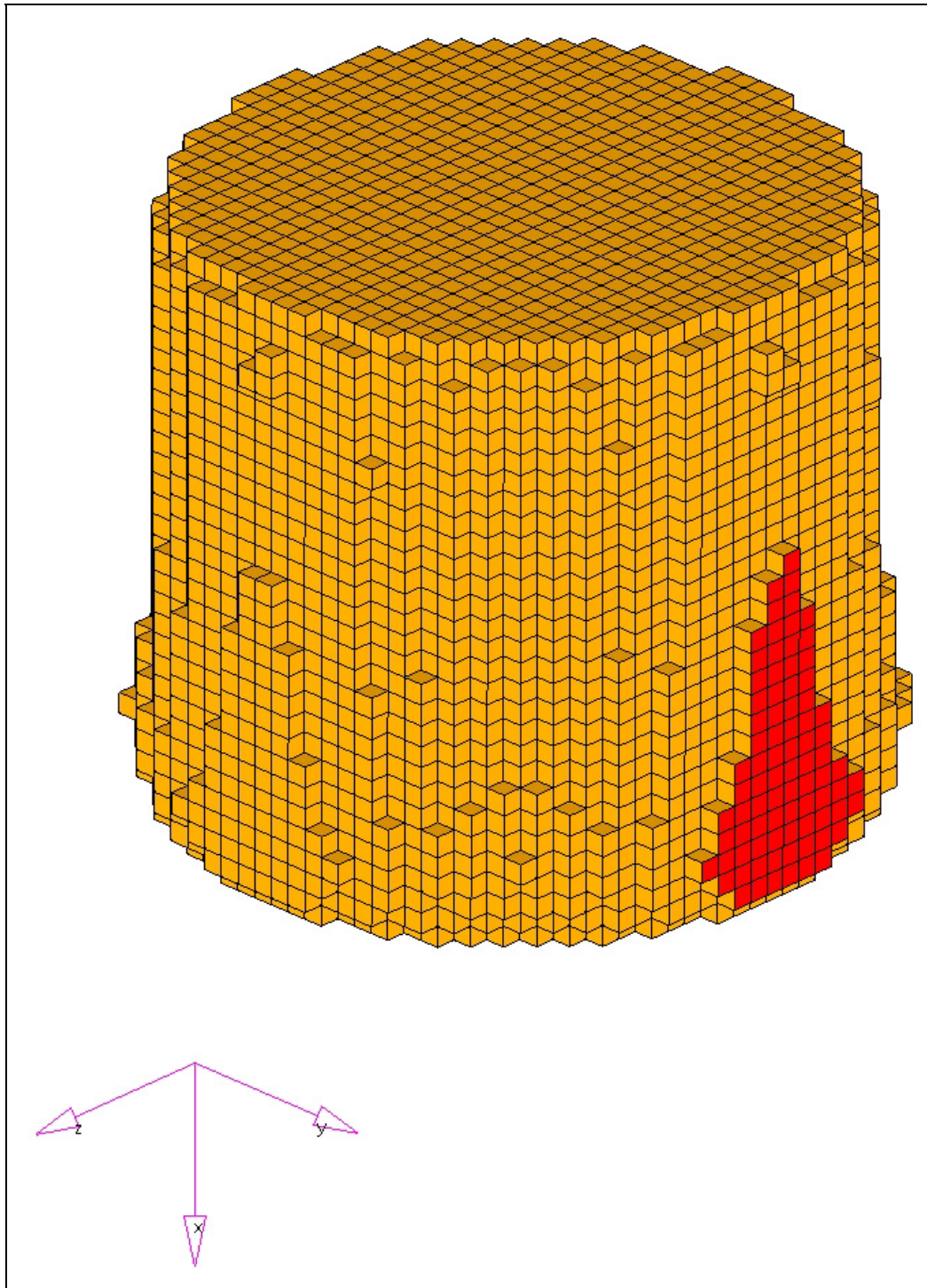
Figure 11. The face of each of 83 residual elements, colored red, was contiguous with the M30 mesh.
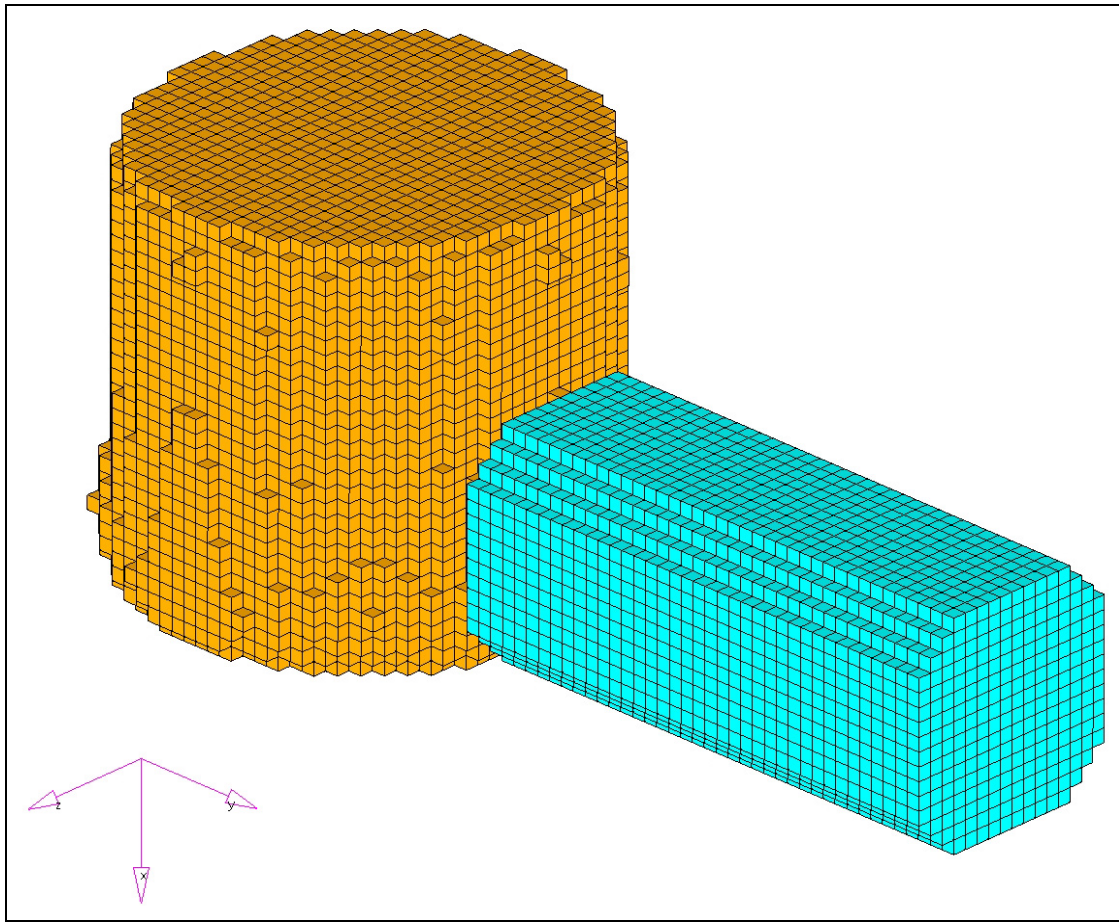
Figure 12. An FE model for a cylindrical grain of M30A1 was generated and placed in contact with the steel residual.
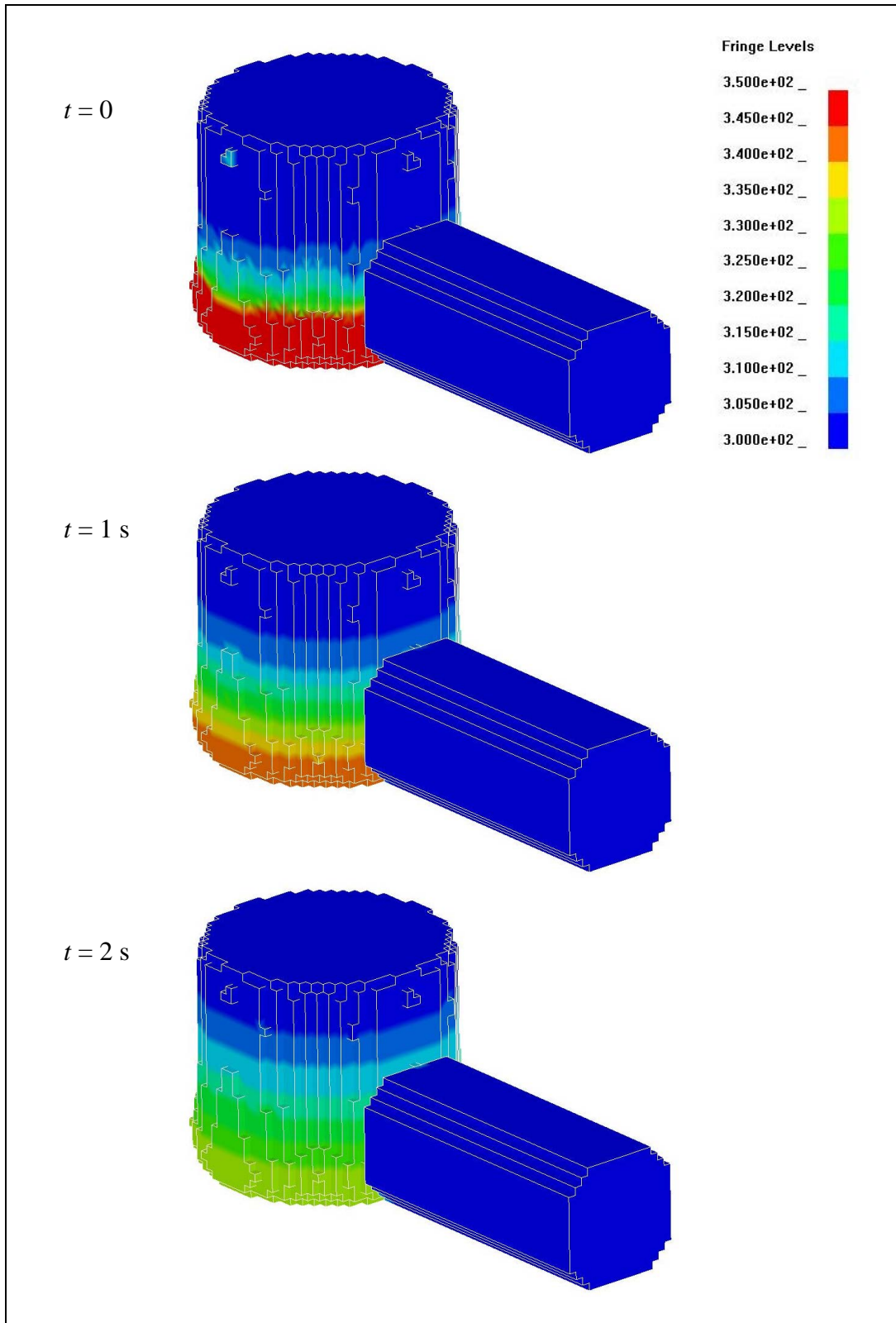
Figure 13. Temperature contours on the outer surfaces of residual and propellant initially and at 1 and 2 s after initial contact. (The fringe levels are in Kelvin.)
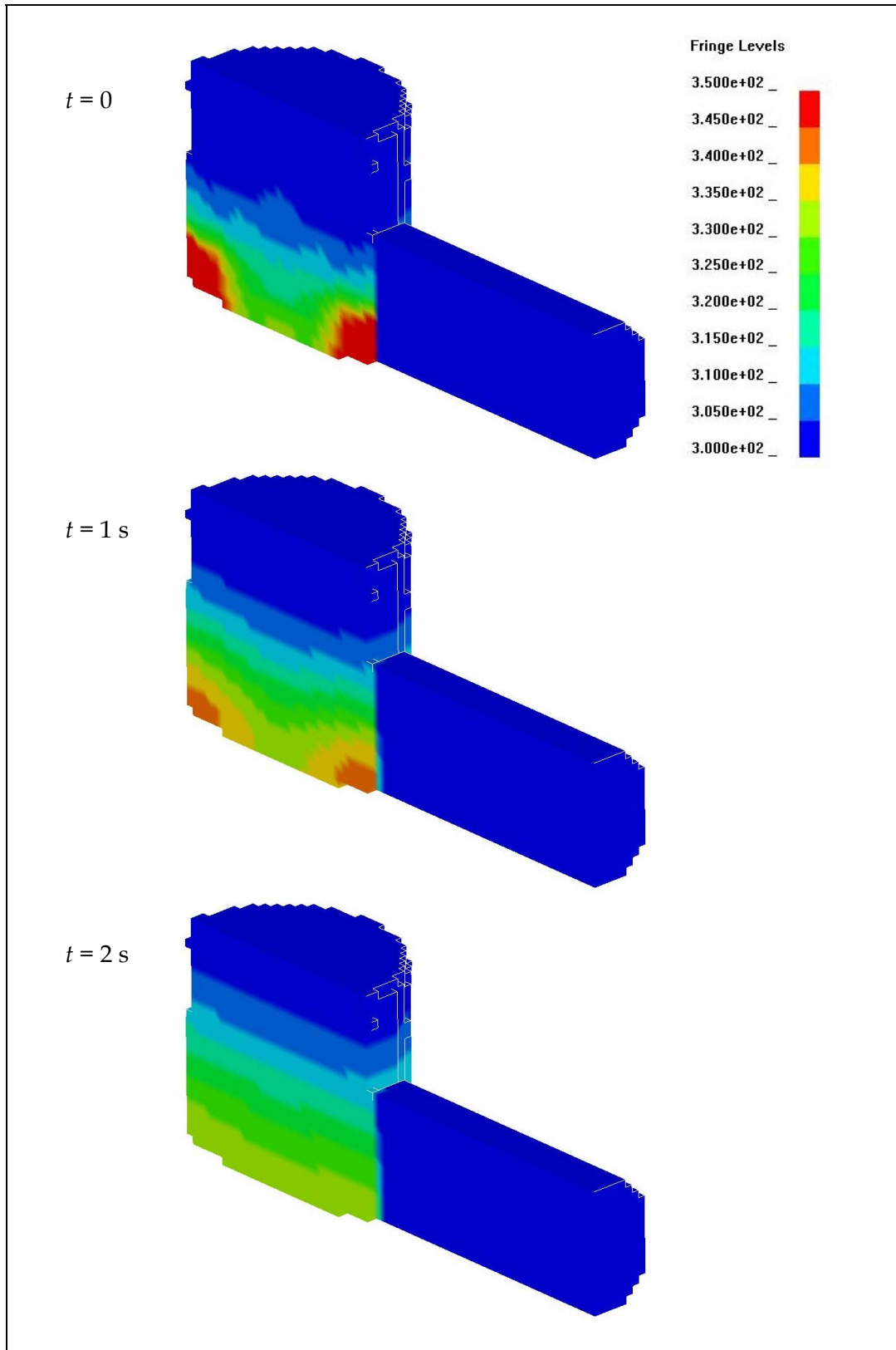
Figure 14. Temperature contours in the midplane of residual and propellant initially and at 1 and 2 s after initial contact. (The fringe levels are in Kelvin.)

Figure 15 identifies five nodes within the diametral plane and at the elevation (*x* location) of the hottest region. The separation between adjacent nodes is the element size, 0.635 mm. The temperature histories of these nodes are shown in figure 16. Nodes *a* and *b*, in the interior of the steel residual, and node *c*, at the residual-grain interface, cool down during the first 0.5 s to a uniform temperature. At 2.4 s, when the calculation was stopped, these nodes are continuing to gradually cool further. Nodes *d* and *e* lie within the propellant grain and heat up over time. There is more disparity between the temperatures of *d* and *e* than between the temperatures of nodes within the steel, indicative of the steel's greater thermal diffusivity.
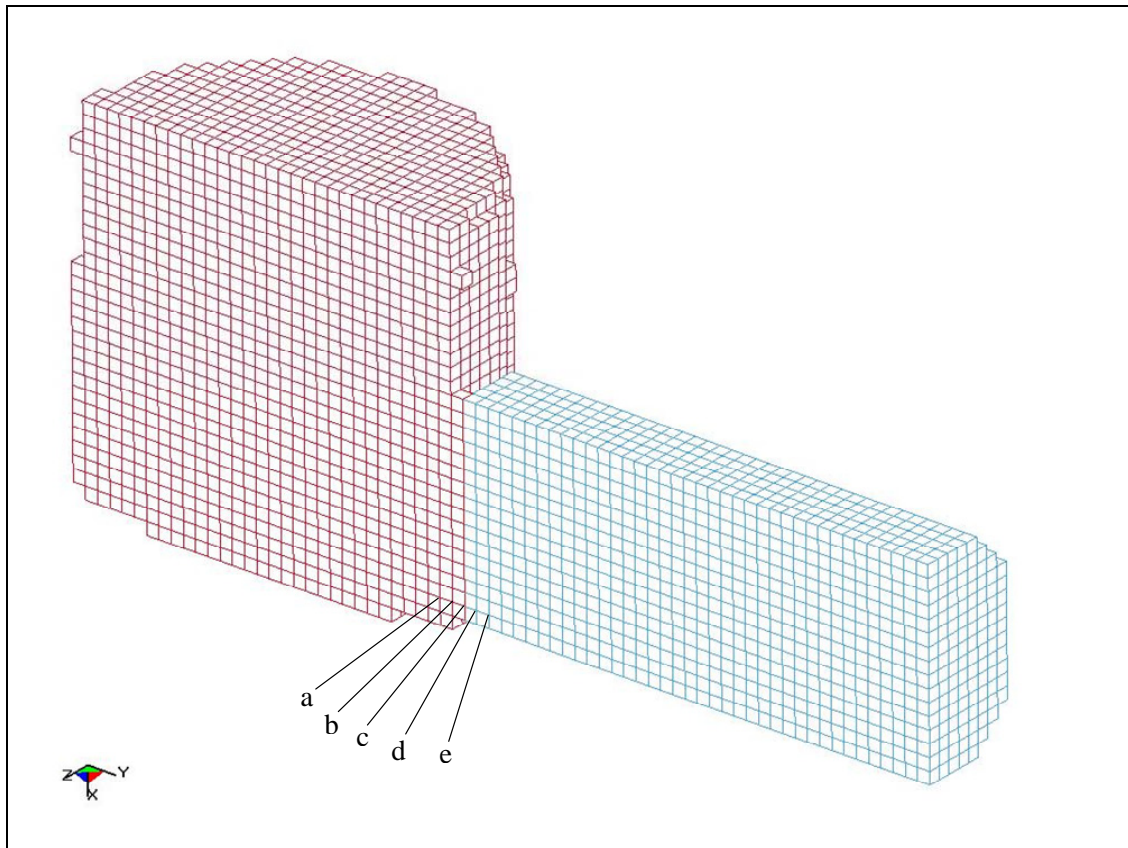
Figure 15. The five nodes at which temperature history is provided in figure 16.
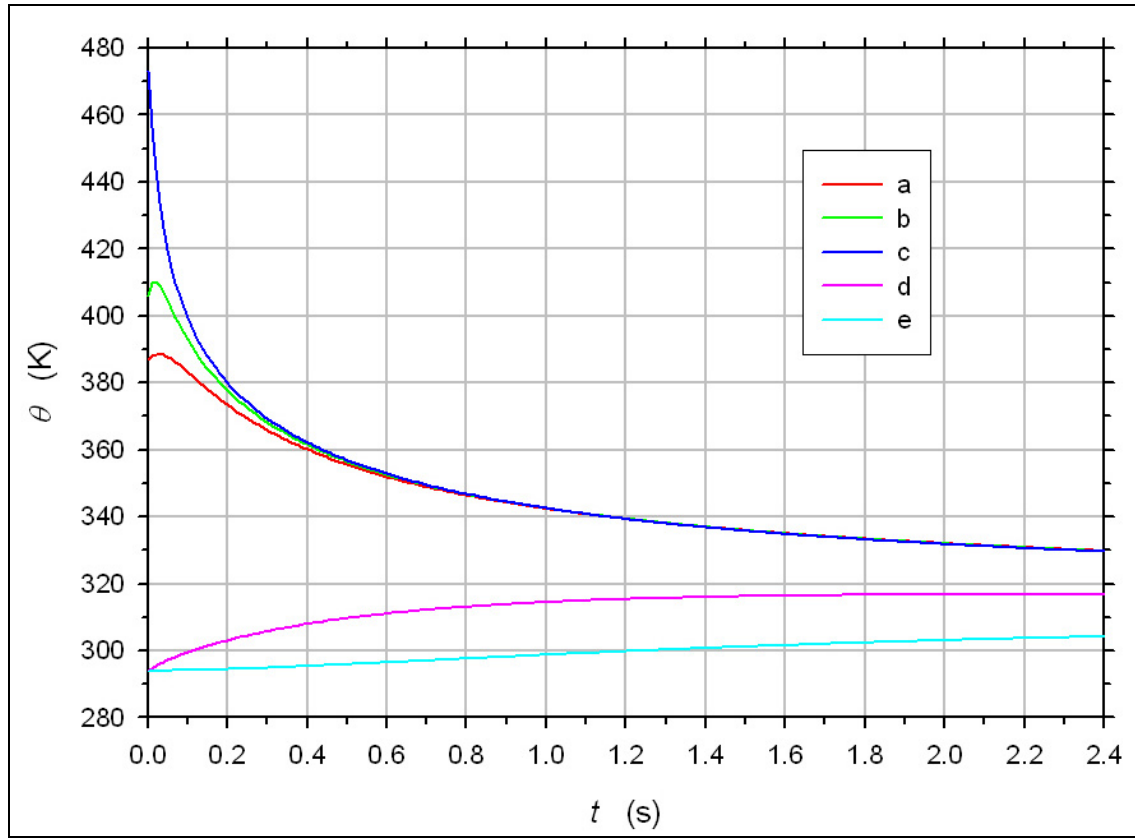
Figure 16. Temperature vs. time at the five nodes identified in figure 15.

Figure 17 shows the initial temperature field on face *A*, the face of the propellant grain in contact with the steel residual. Face *B* is the plane of propellant material recessed one element dimension, 0.635 mm, from face *A*. Nodes 1A–6A are the six hottest nodes in face *A* and are shared by the steel residual. Nodes 1B–6B are their counterparts with the same *x* and *z* coordinates but on face *B*.

Figure 18 shows the computed temperature histories of nodes 1A–6A. These nodes begin at similar temperatures and cool at similar rates. Figure 19 shows temperature histories for nodes 1B–6B. Nodes 1B–6B all start at θ_r and subsequently heat up.

Figure 17. The initial temperature field in the M30A1 grain, and the six nodes at which temperature histories are provided in figure 18. (The fringe levels are in Kelvin.)
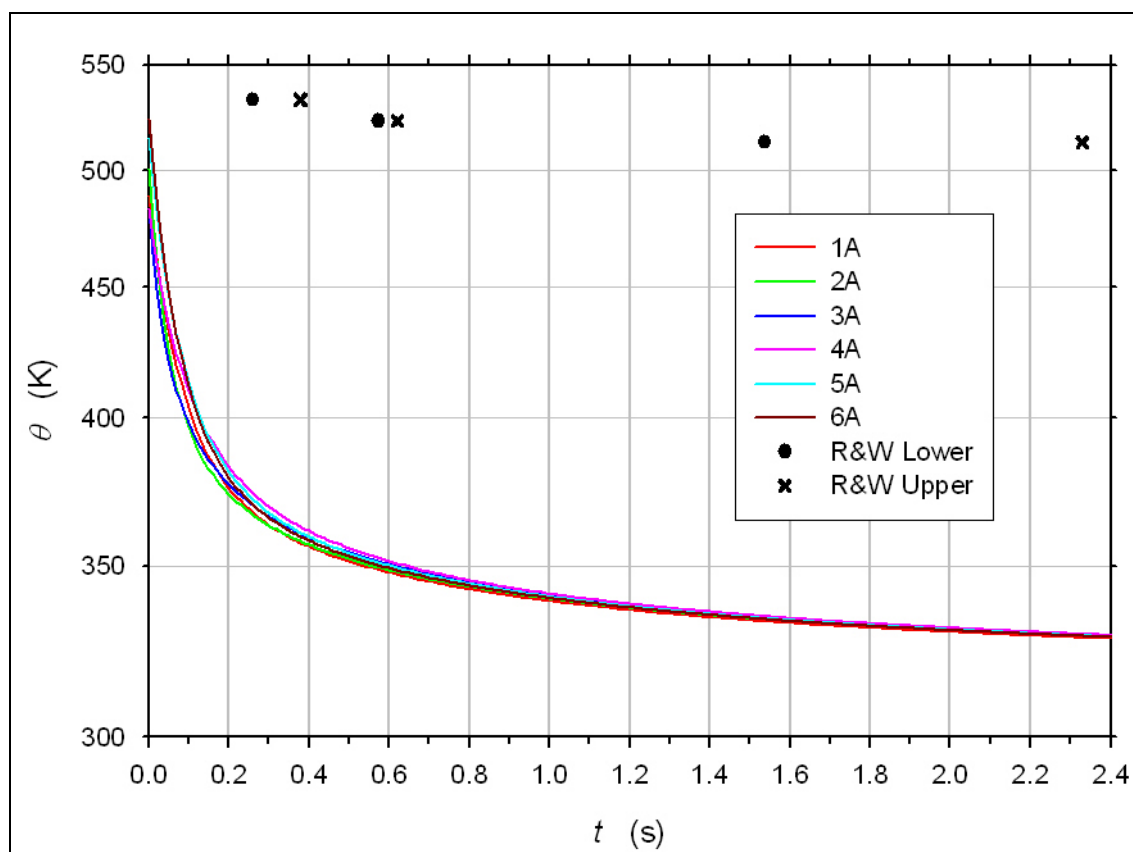
Figure 18. Temperature vs. time at the six nodes identified in figure 17 on face A (the surface in perfect contact with the steel residual), and ignition times reported in Rocchio and Wires (*1*). (Note the logarithmic temperature scale.)
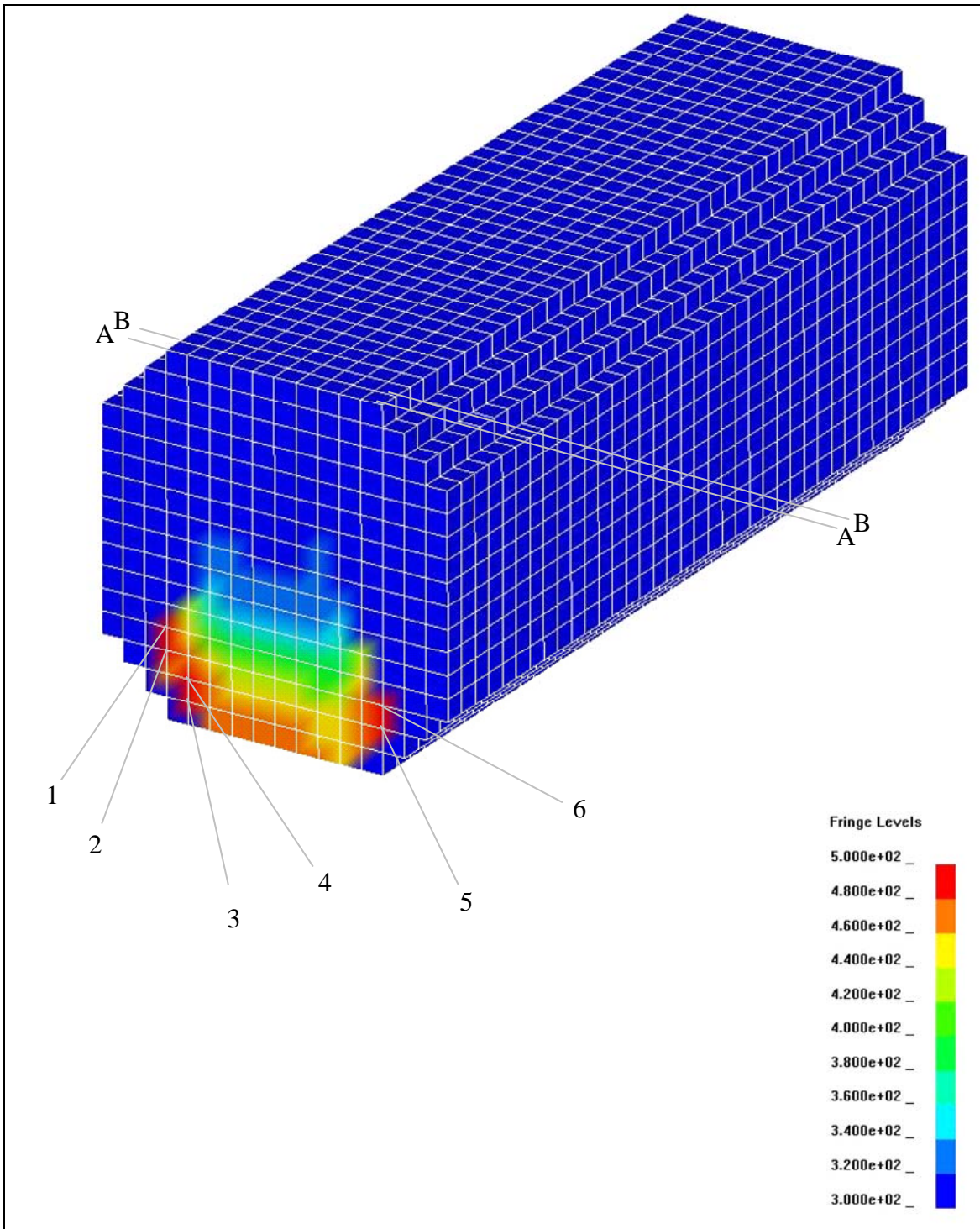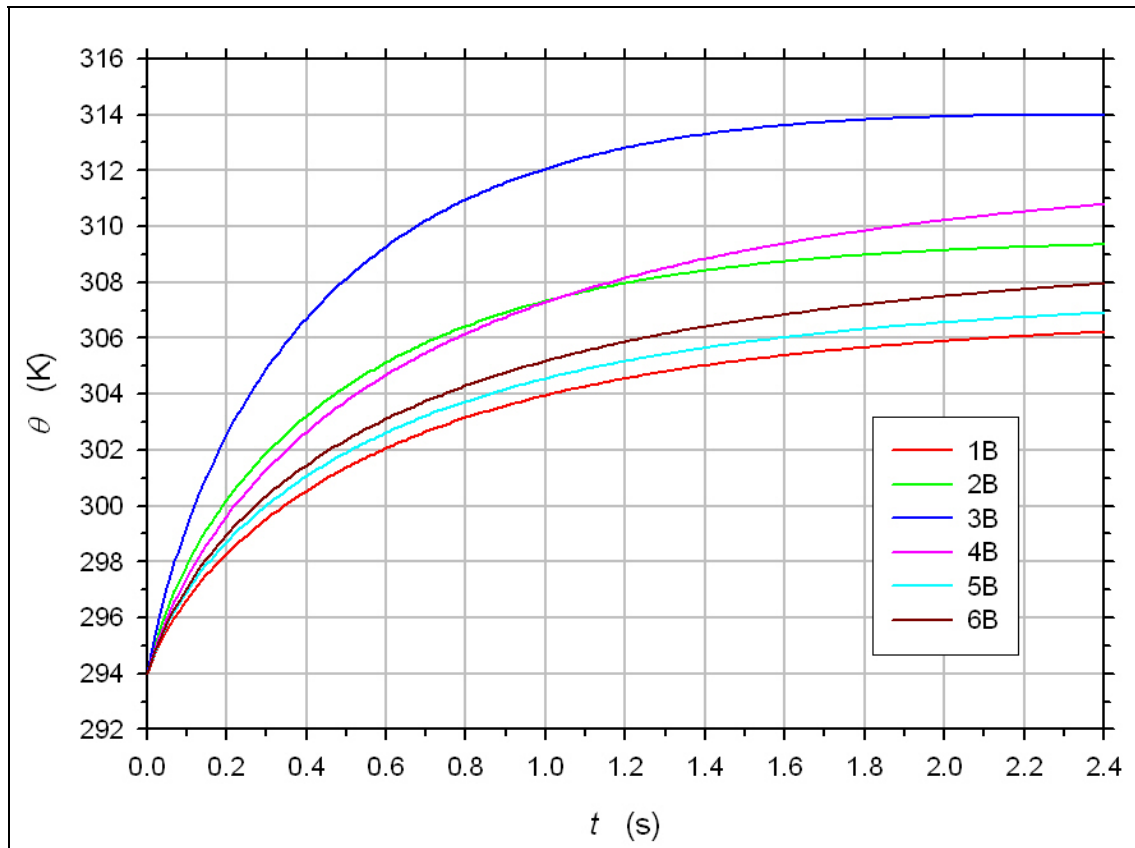
Figure 19. Temperature vs. time at the six nodes identified in figure 17 on face B (the M30 internal plane recessed 0.625 mm from the steel residual).

Figure 20 shows temperature histories for nodes 6A and 6B. Node 6A begins at 524 K. At 2.4 s, temperatures of nodes 6A and 6B have converged to 328 and 308 K, respectively.

Figures 18 and 20 contain data points labeled "R&W Lower" and "R&W Upper." These refer to M30 ignition data reported in Rocchio and Wires (1). Rocchio and Wires performed temperature controlled experiments on single grains of M30. For a range of temperatures between 483 and 533 K, the time required for ignition was measured. Their results, after converting from Celsius to Kelvin, are reproduced in table 4. To quote from Rocchio and Wires (1), "the high limit was that time above which one could always expect sustained combustion and the low limit was that time below which sustained combustion did not occur" (p. 14). These data are the basis for an initiation criterion to apply to the LS-DYNA temperature solution. In figure 18, since all points on curves 6A through 6B lie below the Rocchio and Wires data points, one can conclude that the M30A1 grain that contacts the steel residual in the location and configuration depicted in figures 10–12 will not undergo sustained combustion. Note again that in our analysis the grain did not contact the residual at the latter's hottest location.

25
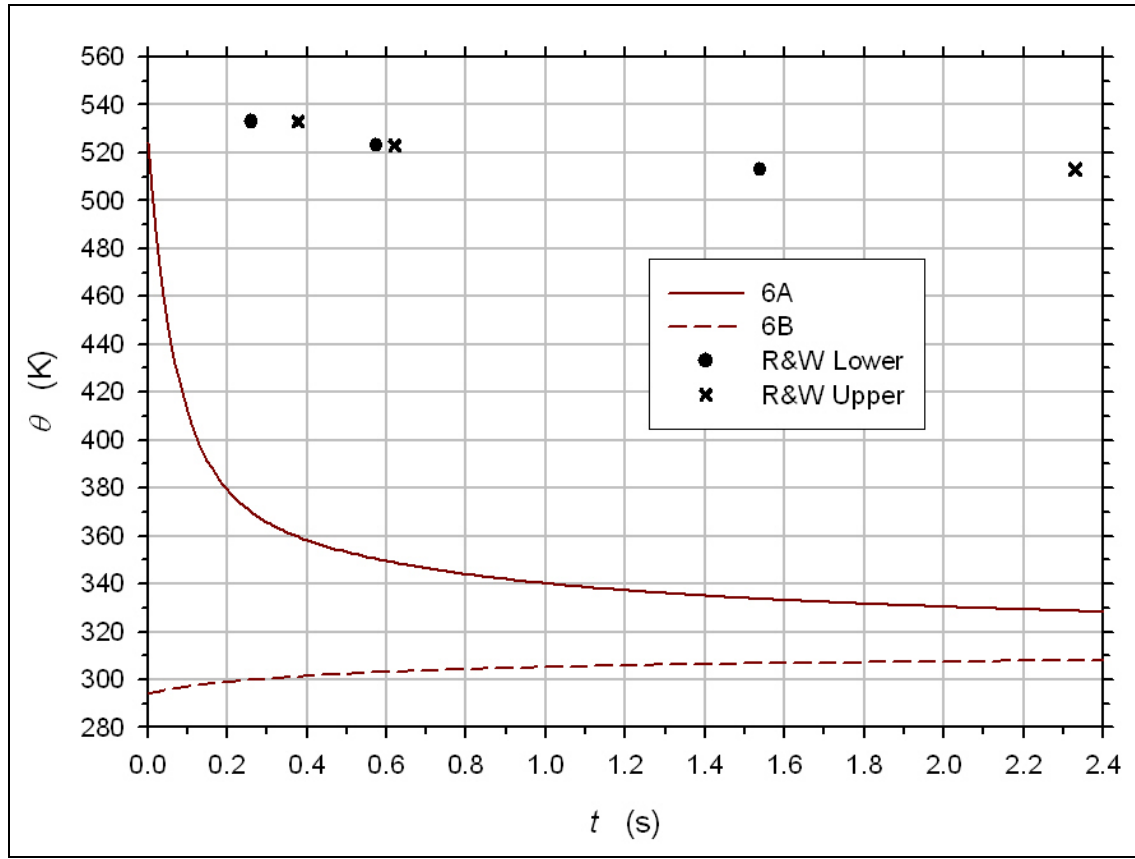
Figure 20. Temperature vs. time at two nodes identified in figure 17, one on face A and one on face B, and ignition times reported in Rocchio and Wires (*1*).

Table 4. Measured times required for sustained combustion as functions of temperature (reproduced from Rocchio and Wires [*1*]).

θ (K)	t_{lower} (s)	t_{upper} (s)
533	0.260	0.378
523	0.574	0.621
513	1.538	2.329
503	3.422	4.111
493	6.257	7.045
483	9.400	18.256

The issue of mesh sensitivity is explored in the appendix. There we study one-dimensional heat conduction between a semi-infinite region of steel, initially at a uniform non-zero temperature, in perfect thermal contact with a semi-infinite region of propellant, initially at zero temperature. First, an analytical solution is obtained. Next, the problem is simulated with LS-DYNA using the same 0.635-mm cubic elements as used in the present section 4. Good agreement between

the analytical and the LS-DYNA solutions in the propellant give some support to the adequacy of the meshing employed here in section 4. Note, however, that the problem solved in the appendix involves a uniform initial temperature throughout the steel, whereas the spatially varying temperature field predicted by CTH introduces additional length scales that can affect mesh adequacy.

5. Concluding Remarks

5.1 Summary

A procedure was developed for performing a postprocessing heat conduction analysis from a CTH solution for a residual penetrator's shape and temperature field. LS-DYNA was employed for the heat conduction analysis. The interface between CTH and LS-DYNA involved the codes EnSight and HyperMesh. Figure 4 schematizes the overview.

The procedure was applied to perforation of a titanium plate by a steel RCC at 433 m/s, followed by cookoff of an M30A1 grain by contact with the hot steel residual. Heat conduction was neglected in the steel-titanium perforation analysis, performed with CTH. Deformation and motion were neglected in the postprocessing heat conduction analysis, performed with LS-DYNA. The temperature field as a function of time within the M30A1 grain was compared with data in Rocchio and Wires (*1*) for initiation time as a function of temperature.

5.2 Assessment

The heat conduction analysis with LS-DYNA was straightforward and presented no special challenges. The main uncertainties were introduced by the perforation analysis with CTH. In particular, the steel and titanium exhibited signs of adiabatic shear banding in associated U.S. Army Research Laboratory Survivability/Lethality Analysis Directorate experiments, and this damage mechanism was not represented in the Johnson-Cook fracture model.

If the steel residual hits the bed of propellant with a substantial velocity, effects occur that were neglected in this analysis. The work performed on the propellant would give rise to additional heating that could contribute to combustion initiation.

6. References

1. Rocchio, J. J.; Wires, R. A. *A Study of the Thermal Initiation, Cookoff, of M30 Propellants*; ARBRL-MR-2847; U. S. Army Ballistic Research Laboratory: Aberdeen Proving Ground, MD, 1978.

2. Bell, R. L.; Baer, M. R.; Brannon, R. M.; Crawford, D. A.; Elrick, M. G.; Hertel, E. S.; Schmitt, R. G.; Silling, S. A.; Taylor, P. A. *CTH User's Manual and Input Instructions*, *Version 7.1*, Sandia National Laboratories: Albuquerque, NM, 2006.

3. Computational Engineering International, Inc., EnSight, version 8.0. http://www.ensight.com.

4. Livermore Software Technology Corporation. *LS-DYNA Keyword User's Manual*, *Version 970*; Livermore, CA, April 2003.

5. Zerilli, F. J.; Armstrong, R. W. Dislocation-Mechanics Based Constitutive Relations for Material Dynamics Calculations. *Journal of Applied Physics* **1987**, *61*, 1816–1827.

6. Johnson, G. R.; Cook, W. H. A Constitutive Model and Data for Metals Subjected to Large Strains, High Strain Rates and High Temperatures. *Proceedings of the 7th International Symposium on Ballistics*, The Hague, 1983, pp 541–547.

7. Johnson, G. R.; Cook, W. H. Fracture Characteristics of Three Metals Subjected to Various Strains, Strain Rates, Temperatures and Pressures. *Engineering Fracture Mechanics* **1985**, *21*, pp 31–48.

8. Steinberg, D. J. *Equation of State and Strength Properties of Selected Materials*; UCMRL−MA−106439; Lawrence Livermore National Laboratory: Livermore, CA, 1996.

9. Kohn, B. J. *Compilation of Hugoniot Equations of State*; UCMRL-MA-106439; U.S. Air Force Weapons Laboratory: Kirtland AFB, NM, 1969.

10. Meyer, H. W.; Kleponis, D. S. Modeling the Height Strain Rate Behavior of Titanium Undergoing Ballistic Impact and Penetration. *International Journal of Impact Engineering* **2001**, *26*, 509–521.

11. Meyer, H. W.; Kleponis, D. S. *An Analysis of Parameters for the Johnson-Cook Strength Model for 2-in-Thick Rolled Homogeneous Armor*; ARL-TR-2528; U. S. Army Research Laboratory: Aberdeen Proving Ground, MD, 2001.

12. Johnson, G. R.; Holmquist, T. J. *Test Data and Computational Strength and Fracture Model Constants for 23 Materials Subjected to Large Strains, High Strain Rates, and High Temperatures*; LA-11463-MS; Los Alamos National Laboratory: Los Alamos, NM, 1989.

13. Bates, K. Aberdeen Proving Ground, MD. Private communication, 2006.

14. Altair Corporation. http://www.altair.com/software/hw_hm.htm (accessed 2005).

15. Horst, A. W.; Kelso, J. R.; White, K. J. Propelling-Charge Temperature Coefficients: Sources of Disparity. *18th JANNAF Combustion Meeting*, Vol. 2, 1980, pp 69–86.

16. Miller, M. S. *Thermophysical Properties of Six Solid Gun Propellants*; ARL-TR-1322; U. S. Army Research Laboratory: Aberdeen Proving Ground, MD, 1997.

INTENTIONALLY LEFT BLANK.

Appendix. Heat Condition Between Two Semi-Infinite Layers, Each Initially at a Uniform Layer

A.1 Problem Statement

Consider two homogeneous, isotropic materials that obey Fourier's law. Material 1 is characterized by density ρ_1, constant-pressure specific heat c_{p1}, and thermal conductivity κ_1. Material 2 is characterized by ρ_2, c_{p2}, and κ_2. These conductivities, densities, and specific heats are assumed to be material constants, independent of temperature. The thermal diffusivities of the two materials, α_1 and α_2, are defined by

$$\alpha_1 = \frac{\kappa_1}{\rho_1 c_{p1}} \tag{A-1}$$

and

$$\alpha_2 = \frac{\kappa_2}{\rho_2 c_{p2}}. \tag{A-2}$$

Figure A-1 shows the one-dimensional problem to be solved. Materials 1 and 2 occupy the semi-infinite regions $x < 0$ and $x > 0$, respectively. Let $\theta_1(x,t)$ and $\theta_2(x,t)$ be the temperature fields within materials 1 and 2, respectively, where t is time. Heat conduction within the two regions is governed by the equations

$$\frac{\partial \theta_1}{\partial t} = \alpha_1 \frac{\partial^2 \theta_1}{\partial x^2}; \ x < 0, \ t > 0 \tag{A-3}$$

and

$$\frac{\partial \theta_2}{\partial t} = \alpha_2 \frac{\partial^2 \theta_2}{\partial x^2}; \ x > 0, \ t > 0. \tag{A-4}$$

Initially, material 1 is at uniform temperature θ_0 and material 2 is at zero temperature. The initial conditions are then

$$\theta_1(x,0) = \theta_0; \ x < 0 \tag{A-5}$$

and

$$\theta_2(x,0) = 0; \ x > 0. \tag{A-6}$$

31

In the figure:

Left region: $\rho_1,\ \kappa_1,\ c_{p1}$

$$\alpha_1 = \frac{\kappa_1}{\rho_1 c_{p1}}$$

$$\theta_1(x,0) = \theta_0$$

Right region: $\rho_2,\ \kappa_2,\ c_{p2}$

$$\alpha_2 = \frac{\kappa_2}{\rho_2 c_{p2}}$$

$$\theta_2(x,0) = 0$$

x

$$\theta_1(0,t) = \theta_2(0,t)$$

$$\kappa_1 \left. \frac{\partial \theta_1}{\partial x} \right|_{x=0} = \kappa_2 \left. \frac{\partial \theta_2}{\partial x} \right|_{x=0}$$
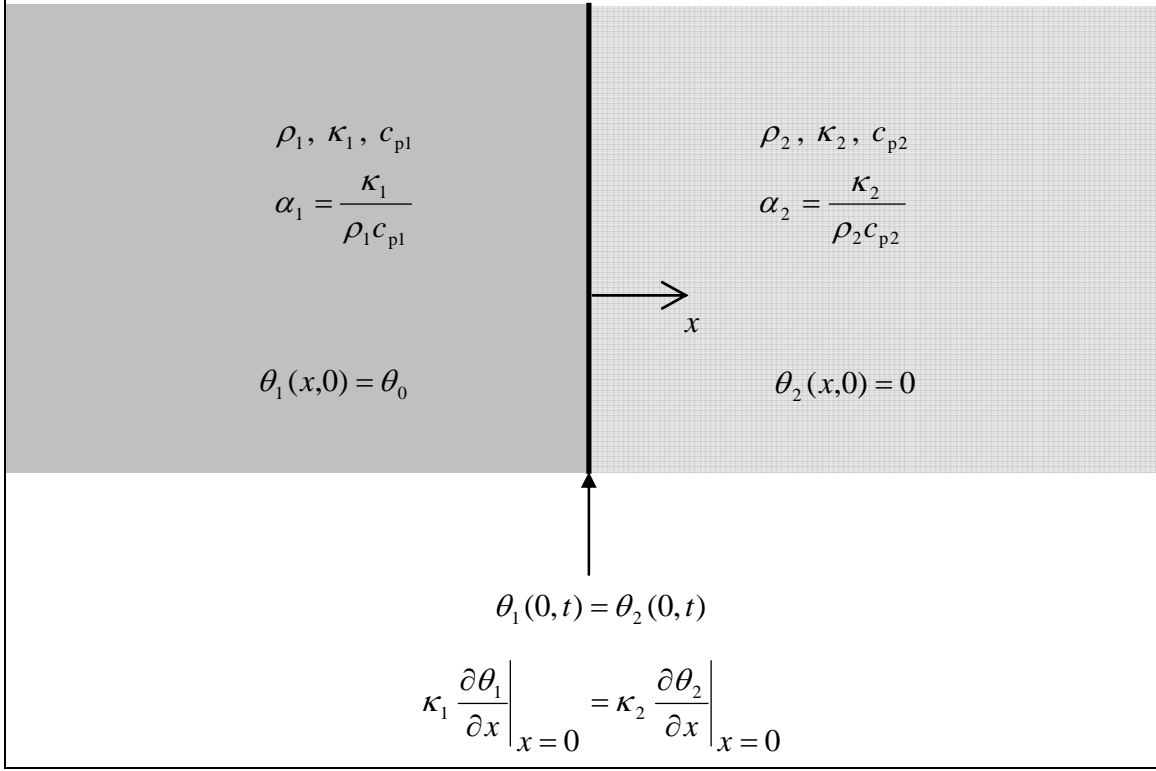
Figure A-1. Problem definition.

Along the interface between steel and propellant, perfect thermal contact is assumed so that temperature and heat flux are both continuous. The interface boundary conditions are

$$\theta_1(0,t) = \theta_2(0,t)\ ;\ t > 0 \tag{A-7}$$

and

$$\kappa_1 \left. \frac{\partial \theta_1(x,t)}{\partial x} \right|_{x=0} = \kappa_2 \left. \frac{\partial \theta_2(x,t)}{\partial x} \right|_{x=0}\ ;\ t > 0. \tag{A-8}$$

Since the domains of materials 1 and 2 are semi-infinite, the remaining boundary conditions are

$$\theta_1(x,t) \to \theta_0 \text{ as } x \to -\infty \tag{A-9}$$

and

$$\theta_2(x,t) \to 0 \text{ as } x \to +\infty. \tag{A-10}$$

A.2 Analytical Solution

The problem can be solved with Laplace transforms. Let $\hat{\theta}_1(x,s)$ and $\hat{\theta}_2(x,s)$ be the Laplace transforms of $\theta_1(x,t)$ and $\theta_2(x,t)$, respectively. These transforms are defined by

$$\hat{\theta}_1(x,s) = \int_0^\infty \theta_1(x,t)e^{-st}dt \tag{A-11}$$

and

$$\hat{\theta}_2(x,s) = \int_0^\infty \theta_2(x,t)e^{-st}dt . \tag{A-12}$$

The Laplace transformations of equations A-3 and A-4 leads to the ODEs

$$\frac{d^2\hat{\theta}_1}{dx^2} - \frac{s}{\alpha_1}\hat{\theta}_1 = -\frac{\theta_0}{\alpha_1} ;\ x < 0 \tag{A-13}$$

and

$$\frac{d^2\hat{\theta}_2}{dx^2} - \frac{s}{\alpha_2}\hat{\theta}_2 = 0 ;\ x > 0 . \tag{A-14}$$

The initial conditions, equations A-5 and A-6, have been absorbed in equations A-13 and A-14.

Laplace transformation of the boundary conditions leads to

$$\hat{\theta}_1(0,s) = \hat{\theta}_2(0,s) ;\ t > 0, \tag{A-15}$$

$$\kappa_1 \frac{d\hat{\theta}_1(x,s)}{dx}\bigg|_{x=0} = \kappa_2 \frac{d\hat{\theta}_2(x,s)}{dx}\bigg|_{x=0} ;\ t > 0, \tag{A-16}$$

$$\hat{\theta}_1(x,s) \to \frac{\theta_0}{s} \ \text{as}\ x \to -\infty, \tag{A-17}$$

and

$$\hat{\theta}_2(x,t) \to 0 \ \text{as}\ x \to +\infty . \tag{A-18}$$

The solution of equations A-13 and A-14 subject to the boundary conditions is

$$\hat{\theta}_1(x,s) = \frac{\theta_0}{s}\left(1 - \frac{K}{1+K}\cdot e^{\sqrt{\frac{s}{\alpha_1}}x}\right) \tag{A-19}$$

and

$$\hat{\theta}_2(x,s) = \frac{1}{1+K}\cdot\frac{\theta_0}{s}\cdot e^{-\sqrt{\frac{s}{\alpha_2}}x} , \tag{A-20}$$

where

33

$$K = \sqrt{\frac{\alpha_1}{\alpha_2}} \cdot \frac{\kappa_2}{\kappa_1} . \tag{A-21}$$

The transforms in equations A-19 and A-20 are inverted using table F-1 in Poulikakos.[1]

$$\theta_1(x,t) = \theta_0 - \frac{K\theta_0}{1+K} \cdot \mathrm{erfc}\left(\frac{-x}{2\sqrt{\alpha_1 t}}\right); \quad x < 0, \ t > 0. \tag{A-22}$$

$$\theta_2(x,t) = \frac{\theta_0}{1+K} \cdot \mathrm{erfc}\left(\frac{x}{2\sqrt{\alpha_2 t}}\right); \quad x > 0, \ t > 0. \tag{A-23}$$

Here, the error function is defined by

$$\mathrm{erf}(\eta) = \frac{2}{\sqrt{\pi}} \int_0^\eta e^{-\xi^2} d\xi, \tag{A-24}$$

and the complementary error function by

$$\mathrm{erfc}(\eta) = 1 - \mathrm{erf}(\eta). \tag{A-25}$$

Equations A-22 and A-23 were evaluated for materials 1 and 2 associated with 4340 steel and M30A1 propellant, respectively. The material constants were assigned the values in table 2. The results are shown in figure A-2. Here, temperature is plotted as a function of time at x locations separated by 0.625 mm. Note that at any given time temperature is much more uniform in the steel than in the propellant due to the steel's greater thermal diffusivity.

A.3 LS-DYNA Simulation

The problem was simulated using LS-DYNA. A single row of 8-node hexagonal brick elements was used (figure A-3). Each element was a cube with a 0.635-mm edge length. These elements were geometrically identical to those used in the 3D analysis of the steel residual and the propellant grain in section 4. Also, the same LS-DYNA thermal material model as in section 4 was employed. The two semi-infinite domains were approximated with 100 elements each, for a total dimension of 63.5 mm each.

Figures A-4 and A-5 compare the LS-DYNA results with the analytical solution in the steel and propellant, respectively. In the steel, the initial cooling is not as rapid in the LS-DYNA solution as in the analytical solution. Note, however, the fine temperature scale in figure A-4. The solution in the propellant is generally more important in a computational scheme to predict propellant initiation, and the LS-DYNA solution in figure A-5 appears to be quite good.

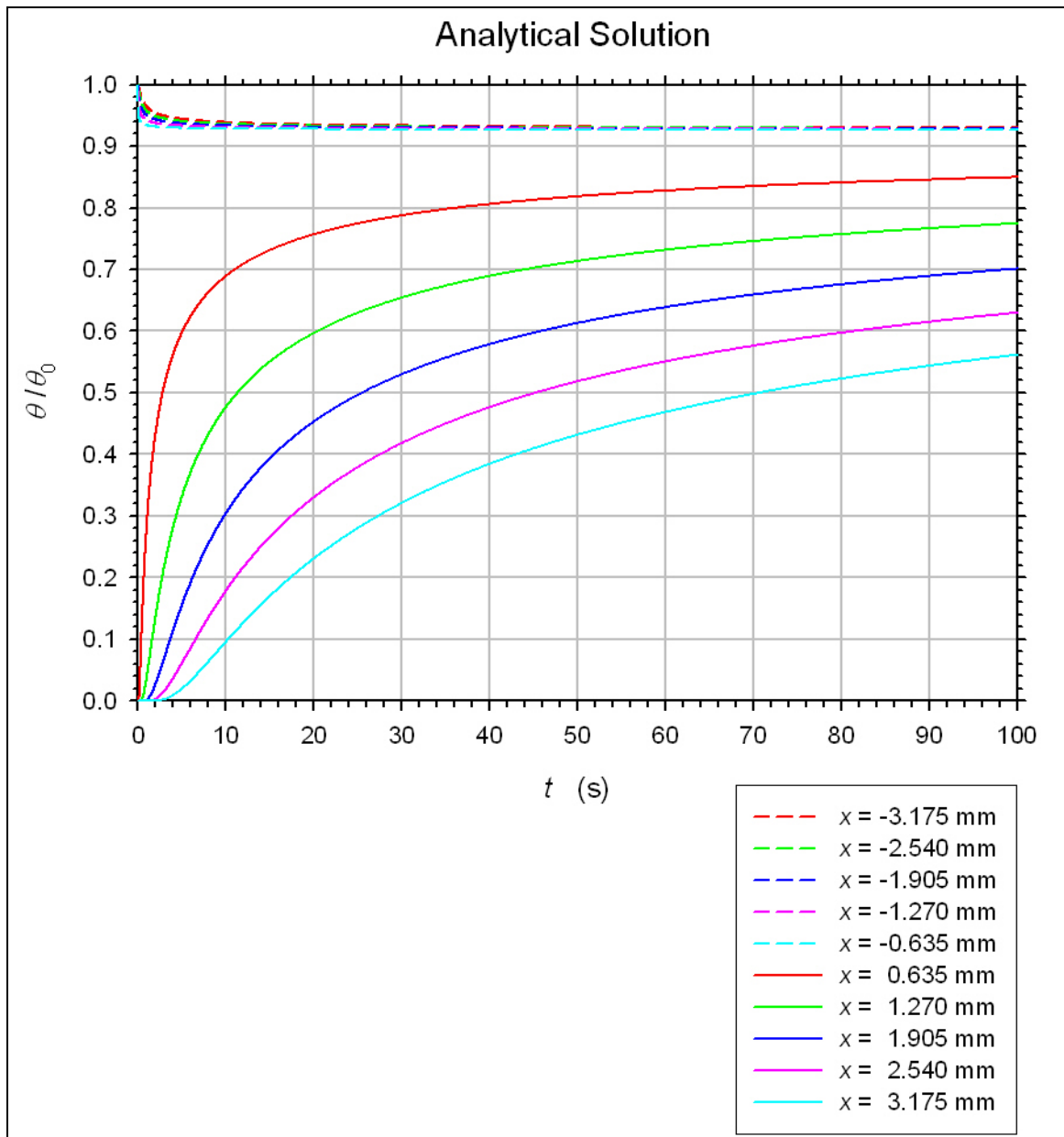[1]Poulikakos, D. *Conduction Heat Transfer*; Prentice Hall: Englewood Cliffs, NJ, 1994.

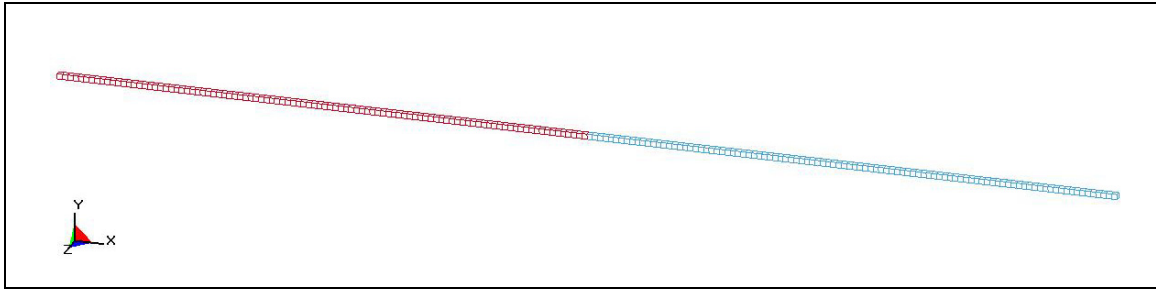Figure A-2. Analytical results for temperature vs. time at the specific locations.
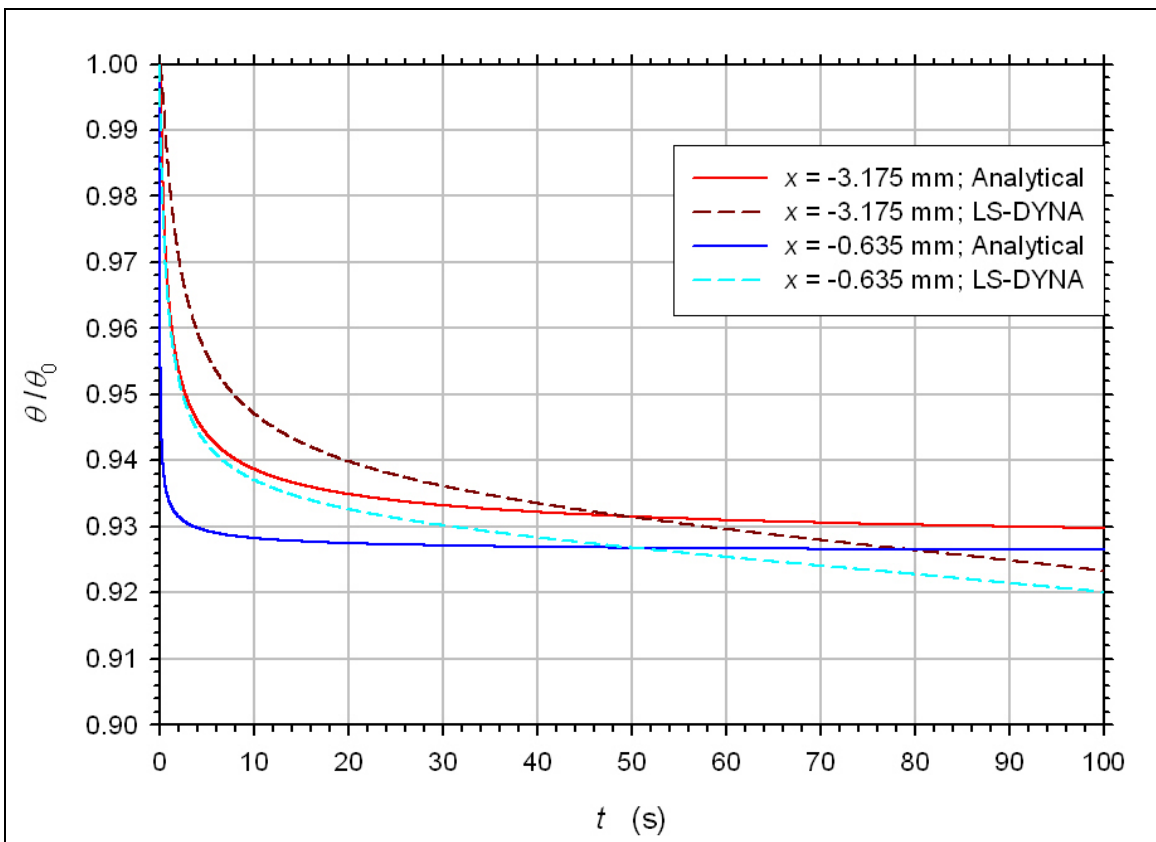
Figure A-3. Mesh used in LS-DYNA simulations.

Figure A-4. LS-DYNA results compared with the analytical solution in the 4340 steel.
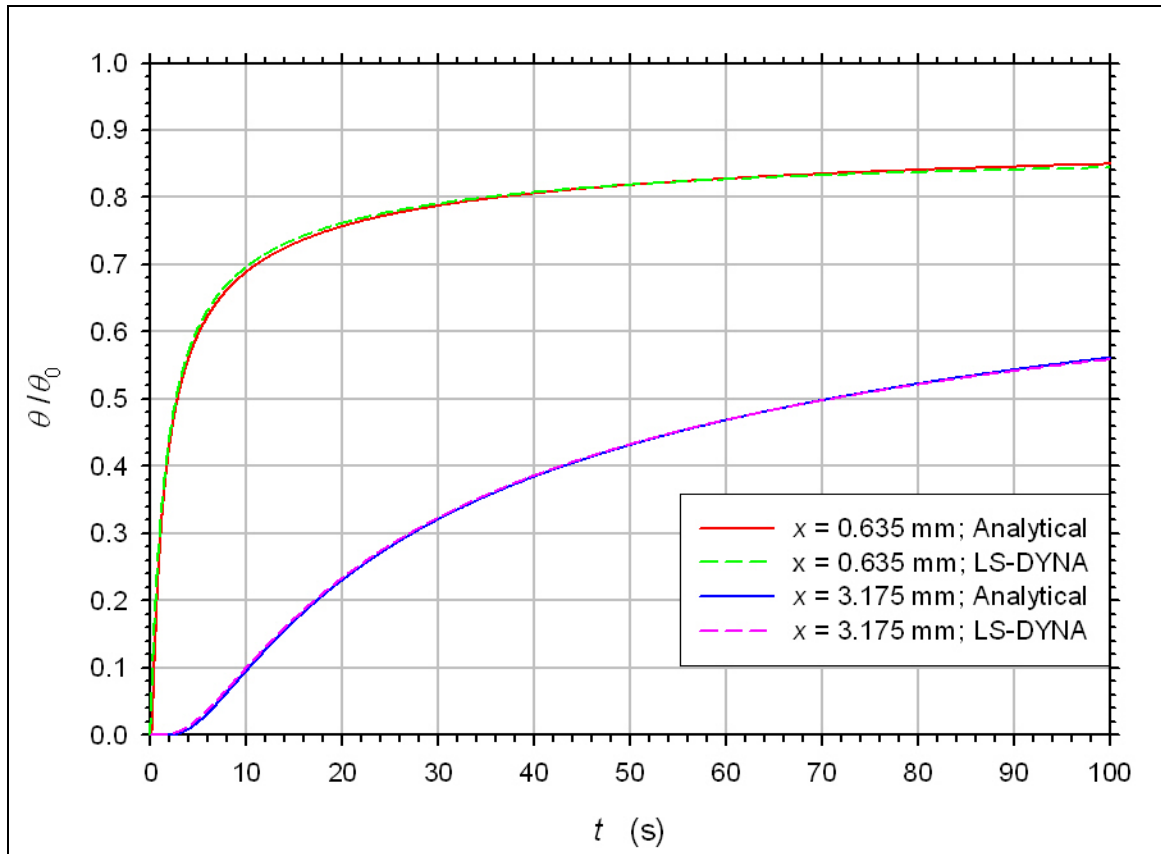
Figure A-5. LS-DYNA results compared with the analytical solution in the M30A1 propellant.

INTENTIONALLY LEFT BLANK.

List of Symbols, Abbreviations, and Acronyms

A, B, C, M, N	constants in the Johnson-Cook strength model
$C_0, \ldots, C_5$	constants in the Zerilli-Armstrong FCC strength model
C_s	sound speed
$D_1, \ldots, D_5$	constants in the Johnson-Cook fracture model
L	rod length
P	pressure
S	proportionality constant in the linear U_s-u_p shock Hugoniot relation
U_s	shock speed
c_p	specific heat at constant pressure
c_{p1}	constant-pressure specific heat in steel residual
c_{p2}	constant-pressure specific heat in M30A1 grain
n_1	coordinate along the outward normal to the steel residual's boundary
n_2	coordinate along the outward normal to the propellant grain's boundary
t	time
t_{lower}	time below which sustained combustion does not occur
t_{upper}	time above which one can always expect sustained combustion
u_p	particle speed
x, y, z	spatial (laboratory) coordinates
$\mathbf{x}$	position vector
α	thermal diffusivity
α_1	thermal diffusivity of steel residual
α_2	thermal diffusivity of M30A1 grain
ε	equivalent plastic strain
$\dot{\varepsilon}$	dimensionless time rate of change of equivalent plastic strain

ε_{ij}	*ij* component of the deviatoric plastic strain tensor
κ	thermal conductivity
κ_1	thermal conductivity of steel residual
κ_2	thermal conductivity of M30A1 grain
ν	Poisson ratio
θ	temperature
θ^*	homologous temperature
θ_0	CTH-determined temperature field in steel residual
θ_1	temperature field in steel residual
θ_2	temperature field in M30A1 grain
θ_m	melt temperature
θ_r	room temperature
ρ	density
ρ_1	density of steel residual
ρ_2	density of M30A1 grain
σ_{eq}	von Mises Cauchy stress
σ_{ij}	*ij* component of the Cauchy stress tensor
σ'_{ij}	*ij* component of the deviatoric Cauchy stress tensor

NO. OF
COPIES   ORGANIZATION

  1   DEFENSE TECHNICAL
(PDF   INFORMATION CTR
ONLY) DTIC OCA
        8725 JOHN J KINGMAN RD
        STE 0944
        FORT BELVOIR VA 22060-6218

  1   US ARMY RSRCH DEV &
        ENGRG CMD
        SYSTEMS OF SYSTEMS
        INTEGRATION
        AMSRD SS T
        6000 6TH ST STE 100
        FORT BELVOIR VA 22060-5608

  1   DIRECTOR
        US ARMY RESEARCH LAB
        IMNE ALC IMS
        2800 POWDER MILL RD
        ADELPHI MD 20783-1197

  3   DIRECTOR
        US ARMY RESEARCH LAB
        AMSRD ARL CI OK TL
        2800 POWDER MILL RD
        ADELPHI MD 20783-1197

       ABERDEEN PROVING GROUND

  1   DIR USARL
        AMSRD ARL CI OK TP (BLDG 4600)

41

1	UNIV OF DAYTON RSRCH INST N S BRAR 300 COLLEGE PARK DAYTON OH 45469-0182
1	APPLIED RSCH ASSOC D E GRADY 4300 SAN MATEO BLVD NE STE A 220 ALBUQUERQUE NM 87110
1	INTERNATL RSCH ASSOC D ORPHAL 4450 BLACK AVE STE E PLEASANTON CA 94566-6145
1	VIRGINIA TECH ENGINEERING SCI & MECH R BATRA 220 NORRIS HALL BLACKSBURG VA 24061
2	JHU MECH ENG K T RAMESH K HEMKER LATROBE HALL 3400 N CHARLES ST BALTIMORE MD 21218
1	NORTH CAROLINA STATE UNIV DEPT MECH AND AEROSPACE ENG M ZIKRY BOX 7910 RALEIGH NC 27695-7910
1	UNIV OF CINCINNATI COLLEGE OF ENGRNG A TABIEI 787 RHODES HALL PO BOX 210070 CINCINNATI OH 45221-0070
2	PURDUE UNIV AEROSPACE ENGRNG W CHEN C T SUN 315 N GRANT ST WEST LAFAYETTE IN 47907-2023
1	CALIFORNIA INST OF TECH AERONAUTICS & APPLIED MECH M ORTIZ PASADENA CA 91125

1	UNIV OF ALABAMA ENGRNG MECH S E JONES PO BOX 870278 TUSCALOOSA AL 34587-0278
1	NORTHWESTERN UNIV MECHANICAL ENGRNG W K LIU EVANSTON IL 60208
1	NORTHWESTERN UNIV CIVIL ENGRNG T BELYTSCHKO EVANSTON IL 60208
1	UNIV OF MISSOURI ROLLA CIVIL ENGRNG DEPT W SCHONBERG ROLLA MO 65409-0030
1	UNIV OF ROCHESTER MECHANICAL ENGRNG D QUESNEL ROCHESTER NY 14627
3	LIVERMORE SOFTWARE TECH CORP J HALLQUIST J DAY M JENSEN 2876 WAVERLY WAY LIVERMORE CA 94550-1740
1	COMPUTATIONAL ENGRNG INTL INC D MCKINNIS 2166 N SALEM ST STE 101 APEX NC 27523-6456

ABERDEEN PROVING GROUND

85	DIR USARL
	AMSRD ARL CI
	  R NAMBURU
	  D GROVE
	  J CLARKE (5 CPS)
	AMSRD ARL B
	  D LYON
	  M ZOLTOSKI
	  S WILKERSON

NO. OF
COPIES ORGANIZATION

   1   DIRECTOR
         US ARMY RSCH LAB
         EUROPEAN RESEARCH OFFICE
         AMSRD ARL RD ER
         S SAMPATH
         PSC 802 BOX 15
         FPO AE 09499-1500

   2   RAFAEL BALLISTICS CTR
         M MAYSELESS
         ZVI ROSENBERG
         PO BOX 2250
         HAIFA 31021
         ISRAEL

   1   UNIV OF WATERLOO
         MECHANICAL ENGNRG
         M J WORSWICK
         200 UNIVERSITY AVE
         WEST WATERLOO
         ONTARIO N2L3G1
         CANADA

   2   FRAUNHOFER-INSTITUT
         ERNST-MACH-INSTITUT
         V HOHLER E STRASSBURGER
         ECKERSTRASSE 4
         79104 FREIBURG
         GERMANY

INTENTIONALLY LEFT BLANK.